Physics of Plasmas

A theory of self-organized zonal flow with fine radial structure in tokamak

Cite as: Phys. Plasmas **24**, 122304 (2017); https://doi.org/10.1063/1.4995302
Submitted: 10 July 2017 . Accepted: 13 November 2017 . Published Online: 12 December 2017

Y. Z. Zhang, Z. Y. Liu, T. Xie, S. M. Mahajan, and J. Liu

A theory of self-organized zonal flow with fine radial structure in tokamak

Y. Z. Zhang,[1] Z. Y. Liu,[2,a)] T. Xie,[3] S. M. Mahajan,[4] and J. Liu[1,2]
[1]*Center for Magnetic Fusion Theory, CAS, Hefei, Anhui 230026, China*
[2]*Department of Modern Physics, University of Science and Technology of China, Hefei, Anhui 230026, China*
[3]*School of Science, Sichuan University of Science and Engineering, Zigong, Sichuan 643000, China*
[4]*Institute for Fusion Studies, University of Texas at Austin, Austin, Texas 78712, USA*

(Received 10 July 2017; accepted 13 November 2017; published online 12 December 2017)

The (low frequency) zonal flow-ion temperature gradient (ITG) wave system, constructed on Braginskii's fluid model in tokamak, is shown to be a reaction-diffusion-advection system; it is derived by making use of a multiple spatiotemporal scale technique and two-dimensional (2D) ballooning theory. For real regular group velocities of ITG waves, two distinct temporal processes, sharing a very similar meso-scale radial structure, are identified in the nonlinear self-organized stage. The stationary and quasi-stationary structures reflect a particular feature of the poloidal group velocity. The equation set posed to be an initial value problem is numerically solved for JET low mode parameters; the results are presented in several figures and two movies that show the spatiotemporal evolutions as well as the spectrum analysis—frequency-wave number spectrum, auto power spectrum, and Lissajous diagram. This approach reveals that the zonal flow in tokamak is a local traveling wave. For the quasi-stationary process, the cycle of ITG wave energy is composed of two consecutive phases in distinct spatiotemporal structures: a pair of Cavitons growing and breathing slowly without long range propagation, followed by a sudden decay into many Instantons that carry negative wave energy rapidly into infinity. A spotlight onto the motion of Instantons for a given radial position reproduces a Blob-Hole temporal structure; the occurrence as well as the rapid decay of Caviton into Instantons is triggered by zero-crossing of radial group velocity. A sample of the radial profile of zonal flow contributed from 31 nonlinearly coupled rational surfaces near plasma edge is found to be very similar to that observed in the JET Ohmic phase [J. C. Hillesheim *et al.*, Phys. Rev. Lett. **116**, 165002 (2016)]. The theory predicts an interior asymmetric dipole structure associated with the zonal flow that is driven by the gradients of ITG turbulence intensity. *Published by AIP Publishing.* https://doi.org/10.1063/1.4995302

I. INTRODUCTION

Discovered via numerical simulations[1–4] in the late 1990s, the zonal flows—shear flows that are symmetric both poloidally and toroidally—are believed to play a key role in L-H transitions in tokamaks.[5–7] Although most theories attempting to isolate the mechanism that excites zonal flows are based on the eigenmode approach,[8–23] there are some that employ the "initial value problem" route.[24,25] In all these theoretical frameworks, it is commonly accepted that zonal flows are closely associated with drift waves in tokamak—in fact, they are the core component of what may be called a zonal flow-drift wave system.[5–7] In the present paper, the term zonal flow is used synonymously with low frequency zonal flow; the geodesic acoustic mode (GAM) will be discussed elsewhere.

The flow-drift wave (F-D) system is a self-consistent state created in following steps: Drift waves, driven by free energy from pressure gradient, generate Reynolds stress, which in turn triggers zonal flows to grow. The growing zonal flows, then, work backwards to modulate the drift waves. The modulation, of course, could be in the amplitude and/or in the phase; it is their combined action that will determine the texture of the final state. Amplitude modulation is dominant in the eigenmode approach (based on linear instabilities). To derive the consequences of pure phase modulation (there is no linear instability), the system should be investigated within a nonlinear framework, posed as an initial value problem. As long as the group velocity in the drift wave energy equation is real and *non-singular*, only the phase modulation is possible. It is precisely the scenario to be studied in the present paper.

To expose the global architecture of theory (possibly, sacrificing quantitative accuracy), we will study a relatively simple model based on Braginskii fluid equations. The zonal flow-drift wave system consists of two basic components: (1) the ion temperature gradient (ITG) linear equation set and (2) the zonal flow equation obtained by surface averaging over the vorticity equation; the latter is assumed to be varying on a slower scale compared to the fast scale ITG mode. It is important to notice that in the ITG equation set, there also exist slow and fast scales; the fast scale characterizes the eigenmode equation, while the amplitude or wave energy equation is on the slow scale. Both equations are derived from the same linear ITG equation set in Sec. II by making use of a multiple scale technique—the so-called derivative expansion.[26] While the two-scale procedures are

a)Author to whom correspondence should be addressed: lzy0928@mail.ustc.edu.cn

routine in plasma physics, its application to the tokamak configuration is quite a bit challenging.

For a tokamak plasma, the calculation of Reynolds stress (in the zonal flow equation) as well as the group velocity in the wave energy equation requires a knowledge of the 2D mode structure, primarily because the toroidal curvature induces linear coupling of drift waves pertaining to each individual rational surface. As a result, a meso-scale structure (enveloping the micro-scale structure of slab model modes) emerges in both the radial and poloidal directions. The envelope is a manifestation of the so-called ballooning effect, historically, studied only in the poloidal direction. However, the conventional ballooning theory,[27–29] despite its success in predicting the eigenmode frequency and growth rate, is incapable of calculating the mode structure necessary for calculating Reynolds stress. It was shown in Ref. 30 that because of the assumed up-down symmetry, the Reynolds stress will be identically zero.

By the same token, in group velocity expressions, the terms containing radial and parallel gradients are found to be more important than the curvature terms. When calculated, using a 2D ITG wave function, they exhibit sharp saw-tooth like variation, a feature essential to many new results of this paper.

Fortunately, the recently developed 2D ballooning theory based on Fourier-ballooning transform,[31] in particular, the weakly asymmetric ballooning theory (WABT),[32] can provide the requisite infrastructure for the zonal flow-ITG architecture. More specifically, one finds that the zonal flow equation is a reaction-diffusion (RD) equation and the ITG wave energy equation is the advection (A) equation; both are on the slow scale and constitute what we will call the reaction-diffusion-advection (RDA) system. The 2D ballooning wave function on the fast scale is an input for calculating Reynolds stress and average of operators over the fast scale. A plausible analytical wave function in the ITG fluid model has been constructed and used for the calculation of Reynolds stress in Ref. 33. The same analytical wave function is also used for calculating operator averages to evaluate the group velocities. In Sec. III, the zonal flow equation with phase modulation by ITG wave energy is given. The analytical expression for static Reynolds stress is drawn from the published literature.[33] The dimensionless form of the RDA system is displayed in Sec. IV which also presents two distinct examples of group velocities leading to two distinct temporal classes of zonal flows: the stationary and the quasi-stationary. More spatiotemporal numerical results for single ballooning rational surface (the rational surface pertaining to the ballooning-like mode which has much wider radial extension than that of a slab mode) are presented and discussed in Sec. V. The emphasis is laid on the physical mechanism leading to the formation of a self-organized spatiotemporal structure. The rationale for treating zonal flow as a local traveling wave and the mechanism triggering intermittent instantons (by zero-crossing of radial group velocity) are also suggested. The results based on spectrum analysis, widely used by experimentalists in *i*-phase discharges,[34–37] are presented in Sec. VI. The selective results from nonlinear coupling of multiple ballooning rational surfaces are offered in Sec. VII. Finally, we give a summary and discussion of main results in Sec. VIII. The major numerical algorithms are described in the Appendixes. In Appendix A, the major steps are given for calculating operator averages over the fast scale contained in group velocities. Appendix B is for the diffusive boundary condition of the zonal flow equation. The numerical algorithm for solving the phase equation in configuration (Fourier) space is described in Appendix C (Appendix D), respectively.

II. ITG WAVE ENERGY EQUATION MODULATED BY ZONAL FLOW

The fluid model for ITG waves under modulation of zonal flow consists of the three linearized moment equations: continuity equation of warm ion fluid, parallel momentum balance equation, and ion pressure evolution equation.[38] In a toroidal coordinate system $(r, \vartheta, \varsigma)$, these are

$$\left(\frac{\partial}{\partial t}+\bar{v}\cdot\nabla\right)\left(1-\rho_s^2\nabla_\perp^2\right)\hat{\varphi}+\left(1+\bar{\eta}_i\rho_s^2\nabla_\perp^2\right)(\boldsymbol{v}_*\cdot\nabla)\hat{\varphi} - 2\rho_s c_s(\boldsymbol{\kappa}\times\boldsymbol{b})\cdot\nabla(\hat{\varphi}+\hat{p})+\nabla_\parallel\tilde{u}_\parallel=0, \tag{1}$$

$$\left(\frac{\partial}{\partial t}+\bar{v}\cdot\nabla\right)\tilde{u}_\parallel+c_s^2\nabla_\parallel(\hat{\varphi}+\hat{p})=0, \tag{2}$$

$$\left(\frac{\partial}{\partial t}+\bar{v}\cdot\nabla\right)\hat{p}+\frac{\bar{\eta}_i v_*}{r}\frac{\partial\hat{\varphi}}{\partial\vartheta}=0, \tag{3}$$

where $\bar{v}\equiv\rho_s c_s\boldsymbol{b}\times\nabla\bar{\varphi}=-\rho_s c_s\bar{E}_r\boldsymbol{e}_\vartheta\equiv\bar{v}\boldsymbol{e}_\vartheta$, $\hat{\varphi}$ $(\bar{\varphi})$ is the dimensionless electric potential of the ITG wave (zonal flow) normalized to electron thermal energy, $\hat{p}$ is the dimensionless ion pressure normalized to electron equilibrium pressure p_e (not ion equilibrium pressure p_i), $\boldsymbol{v}_*\equiv-\rho_s c_s(\boldsymbol{b}\times\nabla\ln n_0)\equiv(\rho_s c_s/L_n)\boldsymbol{e}_\vartheta\equiv v_*\boldsymbol{e}_\vartheta$, $c_s\equiv\sqrt{T_e/m_i}$ is the ion sound speed, $\rho_s\equiv c_s/\omega_{ci}$ is the ion Larmor radius at electron temperature, $\bar{\eta}_i\equiv(1+\eta_i)/\tau_e$, $\tau_e\equiv T_e/T_i$, $\eta_i\equiv d\ln T_i/d\ln n_0$, T_e (T_i) is the electron (ion) temperature, n_0 is the equilibrium density, $\nabla_\perp^2\equiv\partial^2/\partial r^2+(1/r^2)\partial^2/\partial\vartheta^2$, $\nabla_\parallel\equiv\boldsymbol{b}\cdot\nabla=(1/qR)[\partial/\partial\vartheta+q(r)\partial/\partial\zeta]$, q is the safety factor, $\tilde{u}_\parallel$ is the fluctuating fluid parallel velocity, $\boldsymbol{b}$ is the unit vector along the equilibrium magnetic field, and $\boldsymbol{\kappa}$ is the magnetic curvature.

The method of multiple scales can be cast into derivative expansion.[26] To the first order, we have

$$\frac{\partial}{\partial t}\to\frac{\partial}{\partial\tilde{t}}+\varepsilon\frac{\partial}{\partial t}\to-i\omega+\varepsilon\frac{\partial}{\partial t},\quad \frac{\partial}{\partial\boldsymbol{r}}\to\frac{\partial}{\partial\tilde{\boldsymbol{r}}}+\varepsilon\frac{\partial}{\partial\boldsymbol{r}},\quad \hat{\varphi}(t,\boldsymbol{r})\to\bar{\phi}(t,\boldsymbol{r})\hat{\varphi}(\tilde{t},\tilde{\boldsymbol{r}}). \tag{4}$$

$\tilde{t},\tilde{\boldsymbol{r}}$ $(t,\boldsymbol{r})$ denotes the fast scale (slow scale) variables. The factor $\varepsilon\ll1$ is introduced for bookkeeping only. $\hat{\varphi}(\tilde{t},\tilde{\boldsymbol{r}})$ describes the fast scale ITG mode, and $\bar{\phi}(t,\boldsymbol{r})$, as the amplitude of ITG wave under modulation by the zonal flow, varies on the slow scale. In the following, the terms containing zonal flow are treated to be first order quantities. In toroidal coordinate system (r,ϑ,ς), we choose $\hat{\varphi}(\tilde{r},\tilde{\vartheta},\tilde{\varsigma})\equiv\exp(in\tilde{\varsigma}-im\tilde{\vartheta})\sum_l\varphi_l(\tilde{r})\exp(-il\tilde{\vartheta})$ to describe the ITG mode of toroidal mode number n at the rational surface r_j, with (integer) $m\equiv nq(r_j)$, where $q(r_j)$ is the safety factor at r_j, $(\tilde{\vartheta},\tilde{\varsigma})$. Notice

that $\varphi_l(\tilde{r})$ is the 2D ITG wave function in $(\tilde{r}, l)$ representation in which $\nabla_\parallel = i(m\hat{s}(\tilde{r}-r_j)/r_j - l)/qR \equiv i(x-l)/qR$, where $x \equiv \hat{s}nq(r_j)(\tilde{r}-r_j)/r_j = \hat{s}k_\vartheta(\tilde{r}-r_j)$. The following convenient definitions will be used throughout this paper: $y \equiv r_j\vartheta$ implying $\hat{\omega}_{*e} \to iv_*(\partial/\partial\tilde{y} + \varepsilon\partial/\partial y) \equiv \hat{\omega}_{*e,0} + \varepsilon\hat{\omega}_{*e,1}$ and $\hat{\omega}_{*i} \to i\bar{\eta}_i v_*(\partial/\partial\tilde{y} + \varepsilon\partial/\partial y) \equiv \hat{\omega}_{*i,0} + \varepsilon\hat{\omega}_{*i,1}$.

The solution of the two-scale system begins with the pressure evolution equation, followed by parallel momentum equation. Substituting Eq. (4) into Eq. (3) yields

$$\hat{p} = \hat{p}_0 + \varepsilon\hat{p}_1 = -\left[1 + \frac{\varepsilon}{i\omega}\left(\frac{\partial}{\partial t} + \bar{v}\frac{\partial}{\partial\tilde{y}}\right)\right]\frac{\hat{\omega}_{*i}}{\omega}\hat{\varphi}. \tag{5}$$

Up to first order, Eq. (2) combined with Eq. (5) becomes

$$\nabla_\parallel\tilde{u}_\parallel = \left[1 + \frac{\varepsilon}{i\omega}\left(\frac{\partial}{\partial t} + \bar{v}\frac{\partial}{\partial\tilde{y}}\right)\right]\frac{c_s^2}{i\omega}\nabla_\parallel^2\left(1 - \frac{\hat{\omega}_{*i}}{\omega} + \varepsilon\left(\frac{\partial}{\partial t} + \bar{v}\frac{\partial}{\partial\tilde{y}}\right)\frac{i\hat{\omega}_{*i,0}}{\omega^2}\right)\hat{\varphi}. \tag{6}$$

Substituting Eqs. (5) and (6) into Eq. (1) yields the single equation in terms of $\hat{\varphi}$

$$\begin{aligned}&\left[-i\omega + \varepsilon\left(\frac{\partial}{\partial t} + \bar{v}\frac{\partial}{\partial\tilde{y}}\right)\right](1 - \rho_s^2\nabla_\perp^2)\hat{\varphi} + (1 + \bar{\eta}_i\rho_s^2\nabla_\perp^2)(\boldsymbol{v}_*\cdot\nabla)\hat{\varphi} - 2\rho_s c_s(\boldsymbol{\kappa}\times\boldsymbol{b})\cdot\nabla\\ &\quad\times\left[1 - \frac{\hat{\omega}_{*i}}{\omega} + \varepsilon\left(\frac{\partial}{\partial t} + \bar{v}\frac{\partial}{\partial\tilde{y}}\right)\frac{i\hat{\omega}_{*i,0}}{\omega^2}\right]\hat{\varphi}\left[1 + \frac{\varepsilon}{i\omega}\left(\frac{\partial}{\partial t} + \bar{v}\frac{\partial}{\partial\tilde{y}}\right)\right]\frac{c_s^2}{i\omega}\nabla_\parallel^2\left[1 + \frac{\hat{\omega}_{*i}}{\omega} - \varepsilon\left(\frac{\partial}{\partial t} + \bar{v}\frac{\partial}{\partial\tilde{y}}\right)\frac{i\hat{\omega}_{*i,0}}{\omega^2}\right]\hat{\varphi} = 0\end{aligned} \tag{7}$$

with further expansion $\hat{\varphi}(t,\boldsymbol{r}) \to \bar{\phi}(t,\boldsymbol{r})\hat{\varphi}(\tilde{t},\tilde{\boldsymbol{r}})$, $\rho_s^2\nabla_\perp^2 \to \rho_s^2\ [(\partial/\partial\tilde{r} + \varepsilon\partial/\partial r)^2 + (\partial/\partial\tilde{y} + \varepsilon\partial/\partial y)^2]$, and $(\boldsymbol{\kappa}\times\boldsymbol{b})\cdot\nabla \to [\sin\vartheta(\partial/\partial\tilde{r} + \varepsilon\partial/\partial r) + \cos\vartheta(\partial/\partial\tilde{y} + \varepsilon\partial/\partial y)]/R$. Now, it is straightforward to obtain the zeroth and first order equations:

The zeroth order equation is

$$\left\{\rho_s^2\left(\frac{\partial^2}{\partial\tilde{r}^2} + \frac{\partial^2}{\partial\tilde{y}^2}\right) - \frac{\omega + \hat{\omega}_{*e,0}}{\omega + \hat{\omega}_{*i,0}} - \frac{2\hat{\omega}_{de,0}}{\omega} - \frac{c_s^2}{\omega^2}\nabla_\parallel^2\right\}\hat{\varphi}(\tilde{r},\tilde{\vartheta}) = 0, \tag{8}$$

where $\hat{\omega}_{*e,0} \equiv \omega_{*e}(i/nq)\partial/\partial\tilde{\vartheta}$, $\omega_{*e} \equiv -k_\vartheta\rho_s c_s(d\ln n_0/dr)$, $\hat{\omega}_{*i,0} \equiv \omega_{*i}(i/nq)\partial/\partial\tilde{\vartheta}$, $\omega_{*i} \equiv k_\vartheta\rho_s c_s(d\ln p_i/dr)$, and $\hat{\omega}_{de,0} \equiv -i(\rho_s c_s/R)(\sin\vartheta\partial/\partial\tilde{r} + \cos\vartheta\partial/\partial\tilde{y})$. Equation (8) will be treated via the 2D Fourier-ballooning transform. The equation for amplitude evolution is derived from the first order $O(\varepsilon)$ equation

$$\frac{\partial\bar{\phi}}{\partial t} + v_{gr}\frac{\partial\bar{\phi}}{\partial r} + v_{gy}\frac{\partial\bar{\phi}}{\partial y} = -ik_\vartheta\bar{v}\bar{\phi}, \tag{9}$$

where $\bar{\phi}(t,r,y)$ is the amplitude for $\hat{\varphi}(\tilde{r},\tilde{\vartheta})$, and

$$v_{gr} \equiv -\frac{2\rho_s^2\langle K_r\rangle(\omega + v_*\bar{\eta}_i k_\vartheta) + \frac{2\rho_s c_s}{R_0}\left(1 + \frac{\bar{\eta}_i v_*}{\omega}k_\vartheta\right)\sin\vartheta}{1 + \rho_s^2\left(\langle K_r^2\rangle + k_\vartheta^2\right) - \frac{2\rho_s c_s}{R_0}\frac{\bar{\eta}_i v_*}{\omega^2}k_\vartheta(\langle K_r\rangle\sin\vartheta + k_\vartheta\cos\vartheta) - \left(1 + \frac{2\bar{\eta}_i v_* k_\vartheta}{\omega}\right)\frac{c_s^2}{\omega^2}\langle\nabla_\parallel^2\rangle}, \tag{10}$$

$$v_{gy} \equiv \frac{v_*\left[1 - \bar{\eta}_i\rho_s^2\left(\langle K_r^2\rangle + 3k_\vartheta^2\right)\right] - 2\omega\rho_s^2 k_\vartheta - \bar{\eta}_i v_*\frac{c_s^2}{\omega^2}\langle\nabla_\parallel^2\rangle - \frac{2\rho_s c_s}{R_0}\left[\frac{\bar{\eta}_i v_*}{\omega}\sin\vartheta\langle K_r\rangle + \left(1 + 2\frac{\bar{\eta}_i v_*}{\omega}k_\vartheta\right)\cos\vartheta\right]}{1 + \rho_s^2\left(\langle K_r^2\rangle + k_\vartheta^2\right) - \frac{2\rho_s c_s}{R_0}\frac{\bar{\eta}_i v_*}{\omega^2}k_\vartheta(\langle K_r\rangle\sin\vartheta + k_\vartheta\cos\vartheta) - \left(1 + \frac{2\bar{\eta}_i v_* k_\vartheta}{\omega}\right)\frac{c_s^2}{\omega^2}\langle\nabla_\parallel^2\rangle}. \tag{11}$$

In Eq. (9), v_{gr} (v_{gy}) is known as the radial (poloidal) component of group velocity. For waves satisfying dispersion in Fourier space, $D(\omega,\boldsymbol{k}) = 0$, $v_{gr} = (\partial D/\partial k_r)/(\partial D/\partial\omega)$, and $v_{gy} = (\partial D/\partial k_y)/(\partial D/\partial\omega)$. In Eqs. (10) and (11), $K_r \equiv -i(\partial/\partial\tilde{r})$ and $\langle\cdots\rangle \equiv \int d\tilde{r}\hat{\varphi}^*\cdots\hat{\varphi}/\int d\tilde{r}\hat{\varphi}^*\hat{\varphi}$. In terms of the phase (eikonal) $\Theta(r,t) \equiv -i\ln\bar{\phi}(r,t)$, Eq. (9) becomes

$$\frac{\partial\Theta}{\partial t} + v_{gr}\frac{\partial\Theta}{\partial r} + v_{gy}\frac{\partial\Theta}{\partial y} = k_\vartheta\bar{v}. \tag{12}$$

A formal inhomogeneous solution of Eq. (12) is

$$\Theta(r,t) = \rho_s c_s k_\vartheta\int_0^t d\tau\bar{E}_r\left(r - \int_\tau^t ds v_{gr}(\vartheta(s)),\tau\right) \tag{13}$$

with $d\vartheta(s)/ds = v_{gy}(\vartheta(s))/r_j$ and $\vartheta(s=0) = 0$. The phase $\Theta(r,t)$ is shown to be the linear functional of zonal flow. It is important to note that the phase $\Theta(r,t)$ is real for real and regular $v_{gr}(\vartheta)$ and $v_{gy}(\vartheta)$. It simply means that the ITG wave energy is modulated only through the phase; the amplitude modulation is absent since $|\bar{\phi}|^2$ is independent of zonal flow [Eq. (9)]. It is

noticeable that the application of ballooning formalism to zonal flow theory has long been documented in the literature as done by Zonca, Chen, and White.[18]

III. ZONAL FLOW EQUATION, RDA SYSTEM

The zonal flow equation can be obtained from the surface average over the nonlinear vorticity equation (e.g., Refs. 39, 5, 7, 11, and 18)

$$a_{\rm neo}\frac{\partial\bar{v}}{\partial t}+\frac{\partial\Re_{\vartheta,j}(x)}{\partial r}-\mu\frac{\partial^2\bar{v}}{\partial r^2}=0,$$
$$\Re_{\vartheta,j}(x)\equiv-\frac{\rho_s^2c_s^2}{r_j}\oint d\vartheta\frac{\partial\hat{\varphi}}{\partial\vartheta}\frac{\partial\hat{\varphi}}{\partial r}, \tag{14}$$

where $a_{\rm neo}$ describes the possible neo-classical shielding ranging from 1 to $\chi_{\rm neo}$ with $\chi_{\rm neo}\equiv 1.6q^2/\sqrt{\varepsilon}$, $\Re_{\vartheta,j}$ stands for the Reynolds stress pertaining to the rational surface at r_j, $\bar{\mathbf{v}}\equiv\rho_s c_s\boldsymbol{b}\times\nabla\bar{\varphi}\equiv\bar{v}\boldsymbol{e}_\vartheta$ is the zonal flow, and μ is the perpendicular viscosity; for the classical fluid model, $\mu\to\mu_{\rm B}\equiv 3\nu_{ii}\rho_i^2/10$, where ν_{ii} is the ion-ion collision frequency and $\rho_i\equiv\sqrt{T_i/m_i\omega_{ci}^2}$ is the ion Larmor radius.

Following the procedure of Ref. 30 $\Re_{\vartheta,j}$ can be expressed as

$$\Re_{\vartheta,j}(x)=\frac{1}{2}k_\vartheta^2\rho_s^2c_s^2\hat{s}\sum_l S'|\varphi_l(x)|^2,$$
$$S'=\frac{{\rm Im}\left[\eta^2k_*(\lambda_*)\right]}{{\rm Im}\eta^2}+\frac{{\rm Re}\eta^2}{2{\rm Im}\eta^2}\frac{d}{dx}\ln|\varphi_l(x)|^2, \tag{15}$$

where S' stands for the radial variation of phase in the Fourier image of the ballooning wave function. The Reynold stress is significant only for modes with up-down asymmetry like the WABT as well as for modes in vertical ballooning theory (VBT); the latter also known as the "general mode" or "ballooning theory of the second kind."[40] The 2D ITG wave function is precisely the (x,l) image of 2D ballooning wave function $\varphi(k,\lambda)$ via the Fourier ballooning transform.[31–33]

We will begin by summarizing some of the results of calculations already published in Ref. 33. The 2D ITG wave function can be well approximated by an analytical form

$$\varphi(k,\lambda)=\chi(k,\lambda)\Psi(\lambda)=e^{i\eta^2(k-k_*(\lambda_*))^2/2}e^{-in\beta_1\lambda-n\beta_2\lambda^2/2} \tag{16}$$

from which one calculates the ballooning wave function $\bar{\chi}(x-l,\lambda_*)\equiv\int dke^{ik(x-l)}\chi(k,\lambda_*)$, leading to $S'\equiv d\,{\rm Arg}[\bar{\chi}(x-l,\lambda_*)]/dx$. It is noticeable that within the framework of WABT, λ_* is generally complex and depends on both l and x.

This analytical form Eq. (16) is used throughout this paper: for the calculation of Reynolds stress in this section and the averaged wave number, e.g., $\langle K_r\rangle$, in the next. The summation over sidebands is approximately expressed in the analytical formula

$$\Re_{\vartheta,j}(x)\approx k_\vartheta^2\rho_s^2c_s^2\hat{s}\left[\frac{{\rm Im}\left(\eta^2k_*(x_*)\right)}{{\rm Im}\eta^2}-\frac{{\rm Re}\eta^2}{{\rm Im}\eta^2}\frac{(x-x_0)}{{\rm n}\sigma}\right]I(x), \tag{17}$$

where $I(x)\equiv\oint d\vartheta[\hat{\varphi}(r,\vartheta)]^2=\frac{1}{2}\sum_\ell|\varphi_\ell(x)|^2$

$$\approx I(x_0)\exp\left[-\frac{(x-x_0)^2}{{\rm n}\sigma}\right] \tag{18}$$

and $x_0\equiv-{\rm n}({\rm Re}\beta_1+{\rm Im}\beta_1{\rm Im}\beta_2/{\rm Re}\beta_2)-|\eta^2|^2{\rm Im}k_*$ $(-i\beta_1/\beta_2)/{\rm Im}\eta^2$ and $\sigma\equiv|\beta_2|^2/{\rm Re}\beta_2+|\eta^2|^2/({\rm nIm}\eta^2)$. $k_*(x_*)$ is an approximated constant for $k_*(\lambda_*)$.

Apparently, $\Re_{\vartheta,j}(x)$ exhibits the structure of a dipole somewhat contaminated by that of a monopole. Therefore, the radial derivative driving the zonal flow should possess a quadrupole structure. From Eq. (12), one notes that the drift wave amplitude is no longer static as soon as the zonal flow starts to modulate the drift wave. This modulation imparts time dependence to $I(r)\to I(r,t)=I(r)\cos^2(\Theta(r,t))$. It is important to notice that the constant part (1/2) in $\cos^2(\Theta(r,t))$ does not contribute to the radial derivative of total Reynolds stress owing to the cancellation from adjacent rational surfaces ($\partial_r\sum_{j=0,\pm1,\pm2,\ldots}\Re_{\vartheta,j}(r)=0$). At this stage, it is helpful to introduce the concept of equivalent Reynolds stress by phase modulation for a single rational surface expressed by the oscillatory part $\Re_\vartheta(r)\cos(2\Theta(r,t))/2$ even though it is only valid in the equation with a large number of rational surfaces. This equivalent concept makes it easier to analyze the behavior of the eventual contribution from individual rational surfaces. We then write equivalent zonal flow equation pertaining to the single rational surface to be

$$a_{\rm neo}\frac{\partial\bar{v}}{\partial t}+\frac{1}{2}\frac{\partial}{\partial r}\left[\Re_\vartheta(r)\cos\left(2\Theta(r,t)\right)\right]-\mu\frac{\partial^2\bar{v}}{\partial r^2}=0 \tag{19}$$

which is then coupled to Eq. (12) in the real representation. For a given single rational surface, the subscript of Reynolds stress j can be dropped in Eq. (19).

Equation (19) is a generic reaction-diffusion equation, while Eq. (12) is in the form of an advection equation. These two equations constitute what we call an RDA system. It is well known that two coupled reaction-diffusion equations tend to develop a self-organized structure in the nonlinear stage[41,42] (pattern formation). In our RDA system, however, there is only one reaction-diffusion equation, nonlinearly coupled to an advection equation. To explore whether self-organized structures can emerge in such a system, we numerically identify two different temporal processes with very similar spatial structures; these will be discussed in the dimensionless form in Sec. IV. Since the reaction term is localized around the rational surface r_j, the relevant boundary conditions, at a position far away from r_j, pertain primarily to the diffusive part. An analytical solution is worked out in Appendix B.

IV. ZONAL FLOW—A SELF-ORGANIZED PATTERN FORMATION

For the problem of zonal flow driven by turbulence, it is appropriate to assume that at $t=0$, there is no zonal flow and the phase function $\Theta(t=0,x)=0$. As a result, the initial growth is linear in time. The simple linear growth ends before the phase Θ approaches $\pi/4$. The long term behavior

is obtained by numerically solving the set of Eqs. (12) and (19). Equation (19) has the dimensionless form

$$\frac{\partial V(x,\tau)}{\partial \tau}+\frac{1}{2}\frac{\partial}{\partial x}\left[\mathrm{R}(x)\cos\left(2\Theta(x,\tau)\right)\right]=\frac{1}{R_z}\frac{\partial^2 V(x,\tau)}{\partial x^2}, \quad (20)$$

where $R_z \equiv 10\tau_e\omega_{ci}\sqrt{I_{\mathrm{eff}}(x_0)}/3\hat{s}a_{\mathrm{eff}}\nu_{ii}$, the so-called "zonal flow Reynolds number," and $a_\mu \equiv \mu/\mu_{\mathrm{B}}$ a measure of anomaly of perpendicular viscosity to the classical one; $I_{\mathrm{eff}} \equiv I/a_{\mathrm{neo}}$ and $a_{\mathrm{eff}} \equiv a_\mu/a_{\mathrm{neo}}$. The zonal flow speed is normalized to $\bar{v}_z \equiv \rho_s k_\vartheta c_s \hat{s}\sqrt{I_{\mathrm{eff}}(x_0)}$ ($\bar{v} = V\bar{v}_z$), time is normalized to $\omega_Z \equiv \bar{v}_z k_\vartheta$ ($t\omega_Z = \tau$), and the dimensionless Reynolds stress is

$$\mathrm{R}(x) \approx \left[\frac{\mathrm{Im}\left(\eta^2 k_*\right)}{\mathrm{Im}\eta^2}-\frac{\mathrm{Re}\eta^2}{\mathrm{Im}\eta^2}\frac{(x-x_0)}{\mathrm{n}\sigma}\right]\exp\left[-\frac{(x-x_0)^2}{\mathrm{n}\sigma}\right]. \quad (21)$$

The inhomogeneous solution of ITG wave energy equation Eq. (12), i.e., Eq. (13), expressed in dimensionless quantities, becomes

$$\Theta(x,\tau)=\int_0^\tau d\tau' V\left(x-\hat{s}\int_{\tau'}^{\tau} d\sigma \hat{v}_{gr}(\vartheta(\sigma)),\tau'\right), \quad (22)$$

where $\hat{v}_{gr} \equiv v_{gr}/\bar{v}_z$,

$$\frac{d\vartheta(\sigma)}{d\sigma}=\hat{v}_{gy}(\vartheta(\sigma))/(k_\vartheta r_j) \quad (23)$$

and $\hat{v}_{gy} \equiv v_{gy}/\bar{v}_z$.

Equation (20) with the diffusive boundary condition given in Appendix B and Eq. (22) with Eq. (23) constitute a well-posed numerical problem for the RDA system. The solution of such a system depends on the details of the tokamak equilibrium. For demonstrating the working of the system, we choose to analyze an L-mode shot on JET.

The basic equilibrium parameters required for the calculation are listed in Tables I [for zonal flow equation (20)] and II [ITG related parameters required for R(x)]. In addition, the parameter for the mode structure as depicted by η^2 in Eq. (16) could be somewhat different from those calculated in the linear stage. Two typical values are chosen: (a) $\eta^2 = -3 + 3.2i$ and (b) $\eta^2 = -4 + 2i$, which leads to two distinct temporal processes: (a) for quasi-stationary and (b) for stationary. The analytical ITG 2D eigenmode [Eq. (16)] is used to calculate the fast-scale averaged expressions for the three operators $\langle K_r\rangle$, $\langle K_r^2\rangle$, and $\langle\nabla_\parallel^2\rangle$ occurring in the group velocity (see Appendix A).

The zonal flow equation is solved by making use of the Crank-Nicolson method[43] along with the diffusive boundary condition described in Appendix B. For large radial group velocity, the advection equation is highly non-local, and the finite difference method does not apply. Two independent methods, direct integration on Eq. (22) and Fourier method for advection equation corresponding to Eq. (22), are shown in Appendixes C and D, respectively. The results characterizing two distinct temporal processes are shown below in Figs. 1 ($\langle K_r\rangle$, $\langle K_r^2\rangle$, and $\langle\nabla_\parallel^2\rangle$), 2 (for normalized radial, poloidal group velocity, $\hat{v}_{gr}$ and $\hat{v}_{gy}$), and 3 (for spatiotemporal evolution of zonal flow), where (a) [(b)] stands for quasi-stationary [stationary]. It is worth mentioning that these two distinct processes occur for the same set of equilibrium parameters with somewhat different mode structure owing to huge differences in $\hat{K}_\parallel^2(\vartheta)$ as shown in Fig. 1 and in group velocities as shown in Fig. 2. It suggests the significance of correlation between the mode structure and the pattern formation.

In this section, only the stationary process is analyzed in detail. It is caused by zero-crossing of poloidal group velocity. In Fig. 2(b), one can clearly see two zero-crossings, at $\vartheta_1 = 3.288$ and $\vartheta_2 = 4.587$. In fact, these two points have distinct characteristics: ϑ_2 is attractive but ϑ_1 is repulsive. The parameter $\vartheta(t=0) = \pi$ is chosen just a little bit smaller than ϑ_1. As suggested by Eq. (23), positive $\hat{v}_{gy}$ leads to a decrease in ϑ, because $k_\vartheta < 0$. As a result, $\vartheta(\sigma)$ moves to ϑ_2 and then gets stuck there because $\hat{v}_{gy}(\vartheta_2) = 0$. If $\vartheta_2 > \vartheta\ (t=0) > \vartheta_1$, then for negative $\hat{v}_{gy}$, ϑ should increase with t till it meets ϑ_2 and then stays there henceforth. The radial velocity $\hat{v}_{gr}$ then becomes a constant in time implying a stationary process.

TABLE I. Basic equilibrium parameters.

R (m)	a (m)	B (T)	r_j (cm)	$\bar{\eta}_i$	$\hat{s}$
2.96	1	2	60	2.8	0.8
q	T_i (keV)	ν_{ii} (Hz)	ρ_s (mm)	c_s (km/s)	v_* (km/s)
3	1	550	1.2	240	1.216

TABLE II. Partial mode related parameters.

n	k_ϑ (/cm)	$k_*(x_*)$	β_1	β_2	σ
−80	−4	$-0.00436-0.0221i$	$0.17+0.0401i$	$0.201-0.1i$	0.353
x_0	ω (kHz)	$I_{\mathrm{eff}}(x_0)$	a_{eff}	$\bar{v}_z$ (m/s)	ω_z (kHz)	R_z
−11.6	−300	10^{-6}	3	−92.16	36.86	275.42

V. MORE SPATIOTEMPORAL NUMERICAL RESULTS

To help us understand how the self-organized structures are formed, we will display the data on the zonal flow $\bar{v}(r,t)$ (Fig. 3) and the phase function $\Theta(r,t)$ in different ways for the quasi-stationary as well as stationary processes.

A. Spatial structure of zonal flow at three time points

The spatial structure of zonal flow $\bar{v}(r,t)$ and phase function $\Theta(r,t)$ is presented in Fig. 4 for three specific time points: $t = 20, 40, 60$ ms. The quadrupole structures are seen very clearly for stationary and quasi-stationary processes. In fact, the movie file (quasi-stationary process only) is available in the caption of Fig. 4 (Multimedia view) for readers to view the time evolution of zonal flow and phase function in configuration space (within the reaction region for zonal flow and beyond for the phase function).

The movie visually suggests that zonal flow is a traveling wave in finite space or a local traveling wave. As shown in Fig. 4(a), for example, the zonal flow is characterized by a central high peak escorted by two sub-dominant peaks on

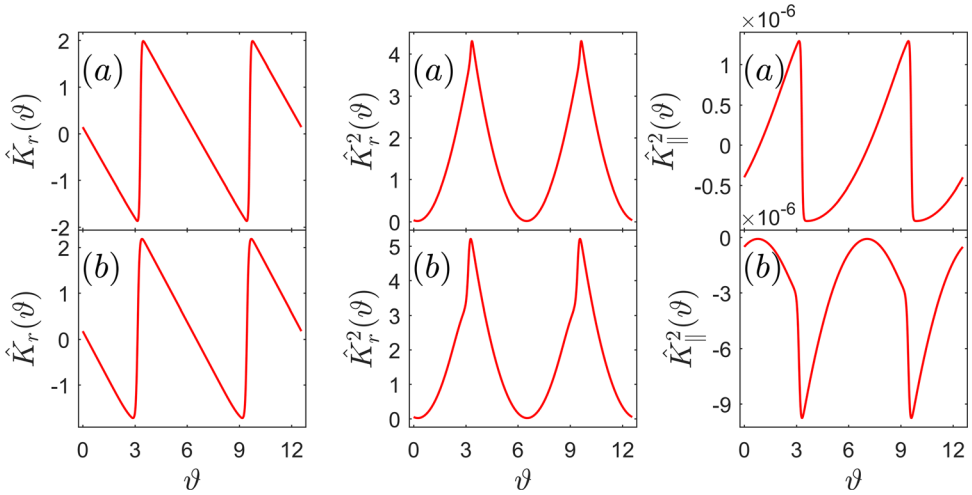

FIG. 1. $\hat{K}_r \equiv \langle K_r \rangle / k_\vartheta$, $\hat{K}_r^2 \equiv \langle K_r^2 \rangle / k_\vartheta^2$ and $\hat{K}_\parallel^2 \equiv \langle \nabla_\parallel^2 \rangle / k_\vartheta^2$ versus ϑ (a) quasi-stationary and (b) stationary.

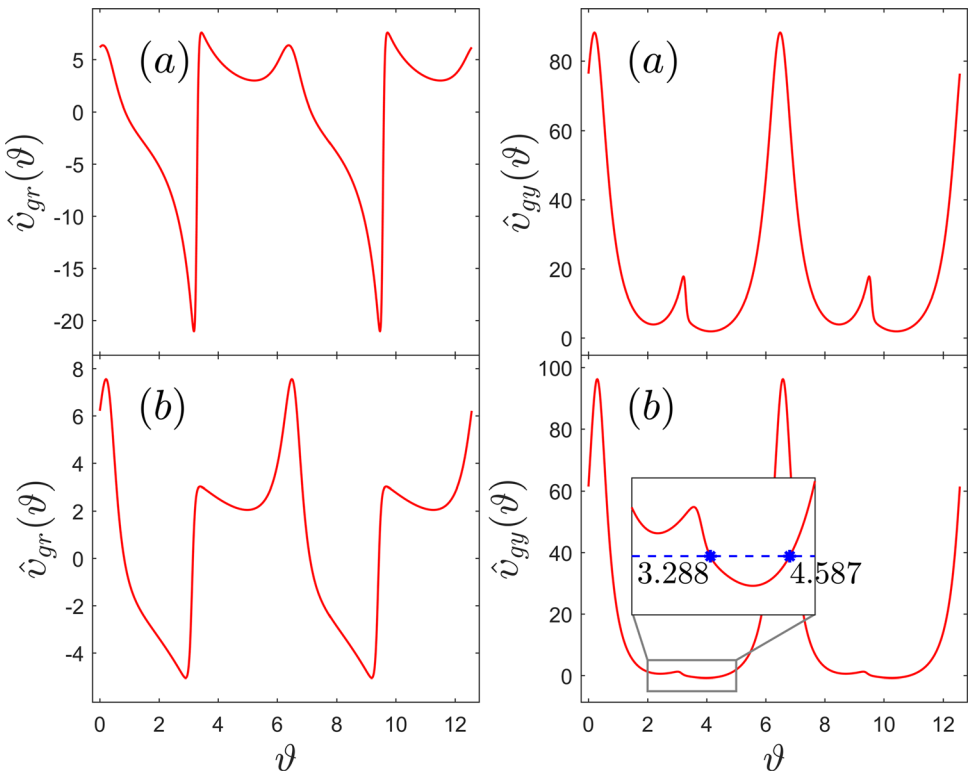

FIG. 2. Normalized radial and poloidal group velocities $\hat{v}_{gr}$ and $\hat{v}_{gy}$ versus ϑ (a) quasi-stationary and (b) stationary.

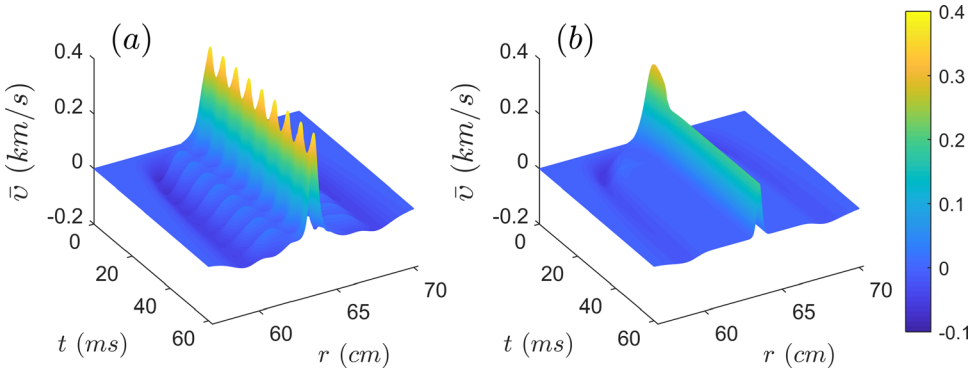

FIG. 3. Spatiotemporal evolution of zonal flow (a) quasi-stationary and (b) stationary.

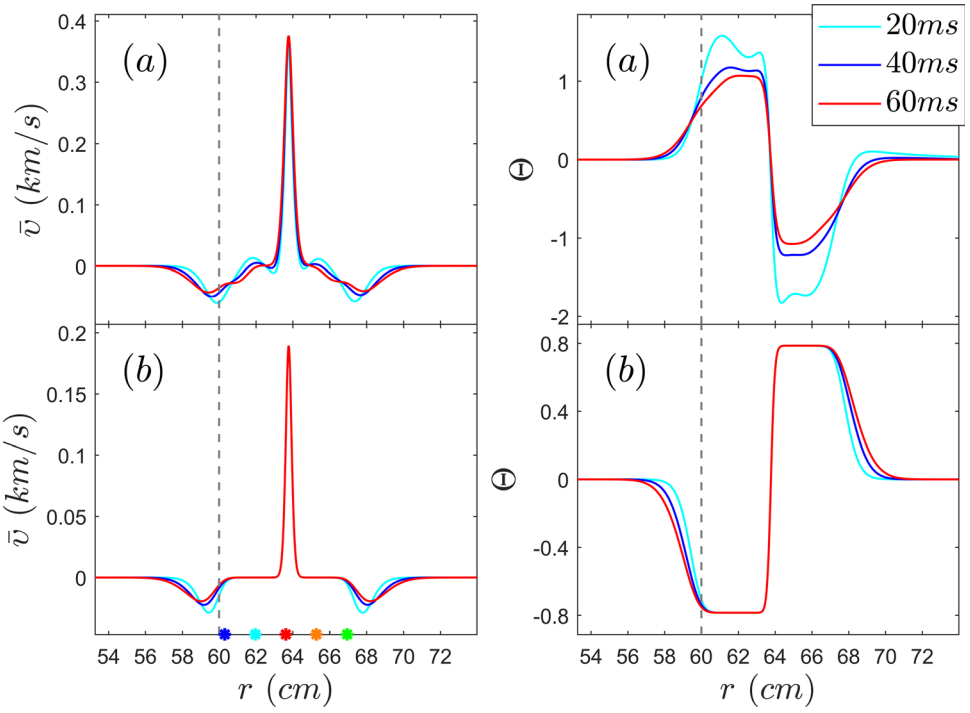

FIG. 4. The spatial structure of zonal flow $\bar{v}(r,t)$ and phase function $\Theta(r,t)$ at three distinct time points at $t = 20, 40, 60$ ms for (a) quasi-stationary and (b) stationary. The time evolution for (a) in $t = [0, 15]$ ms can be seen via the link zonal flow-phase evolution. Multimedia view: https://doi.org/10.1063/1.4995302.1

either side, followed by two valleys that gradually die away. This dynamic signifies a simple breathing of peaks and valleys without any long-range propagation. On the contrary, the long-range propagation is seen clearly in the "motion" of the phase function. One may notice that the signal of phase function could propagate far beyond the meso-scale distance, denoted symbolically by $x_{\pm\infty}$. A cut-off has been introduced somewhere $(\Theta(x_{\pm\infty},\tau) = 0)$ far away from the reaction region. The breathing of peaks and valleys of zonal flow characterizes a motion pattern of the local traveling wave. In terms of Fourier representation, two peaks of the wave number of zonal flow are shown clearly pointing to the opposite direction in Figs. 11 and 13.

When viewing Fig. 4 for zonal flow, one may have also noticed that the sign of zonal flow is varying. Surely, it is a consequence of the fact that the radial average of zonal flow is zero. That is, $\int_{x_{\min}}^{x_{\max}} dxV(x,\tau) = 0$ is a constant of motion according to Eq. (20) for initial zero zonal flow, where $x_{\min}(x_{\max})$ is the in left (right) diffusive region, and $V(x_{\max},\tau) \approx V(x_{\min},\tau) \approx 0$. The numerical work confirms the condition, yielding $\int_{x_{\min}}^{x_{\max}} dxV(x,\tau) / \int_{x_{\min}}^{x_{\max}} dx|V(x,\tau)| < 10^{-6}$.

B. Time evolution of zonal flow and phase function at five spatial points

In this sub-section, we will dwell on the temporal evolution of the zonal flow and the phase function. In Fig. 5, we display the time history of these quantities corresponding to five distinct spatial positions marked blue to green in Fig. 4, i.e., $r_{j,-2} \equiv r_j + \left(x_0 + 2\sqrt{n\sigma}\right)/\hat{s}k_\vartheta$ (dark blue), $r_{j,-1} \equiv r_j + \left(x_0 + \sqrt{n\sigma}\right)/\hat{s}k_\vartheta$ (cyan), $r_{j,0} \equiv r_j + x_0/\hat{s}k_\vartheta$ (red), $r_{j,+1} \equiv r_j + \left(x_0 - \sqrt{n\sigma}\right)/\hat{s}k_\vartheta$ (brown), and $r_{j,+2} \equiv r_j + \left(x_0 - 2\sqrt{n\sigma}\right)/\hat{s}k_\vartheta$ (green). Among others, $r_{j,0}$ corresponds to the position of the central peak of the quadrupole part as the radial derivative of static Reynolds stress, and $r_{j,\pm1}$ corresponds to the two peaks of the dipole part of the static Reynolds stress.

One cannot fail to notice the correlation between the kink in zonal flow $\bar{v}$ and the spike of phase function Θ [Fig. 5(a)]. The zonal flow and the phase function vary smoothly over most of the time. However, at some instants, a kink in the zonal flow appears, simultaneously, with a spike in the phase function. In other words, one may divide the temporal evolution of phase function into two regimes, smooth and spiky. In the smooth regime, a large radial group velocity takes the argument of zonal flow in Eq. (22) into the diffusive region where Reynolds stress is small. When the shift induced by radial group velocities $\hat{s}\int_{\tau'}^{\tau} d\sigma \hat{v}_{gr}(\vartheta(\sigma))$ is comparable to the radial positions x, however, the argument of zonal flow of Eq. (22) falls into the reaction region where Reynolds stress is not small. Our results indicate that the latter occurs very rapidly.

C. Correlation between occurrence of spikes and zero-crossing of radial group velocity

In order to demonstrate the correlation between the occurrence of spikes and zero-crossing of radial group velocity, the first 15 ms portion in Fig. 5(a) is magnified and displayed in Fig. 6 that also shows the time evolution of radial group velocity. The occurrences of four kinks in zonal flow and four spikes in phase function are found to be correlated with the moment at zero-crossing of radial group velocity—marked by event numbers 1, 2, 3, and 4. For events 1 (at $t_1 = 4.4$ ms) and 3 (at $t_3 = 11.2$ ms), the radial group velocity goes from negative to positive, while for events 2 (at $t_2 = 6.7$ ms) and 4 (at $t_4 = 13.5$ ms), it goes from positive to negative; the former (latter) will be called up-zero-crossing (down-zero-crossing). The time evolution around the four

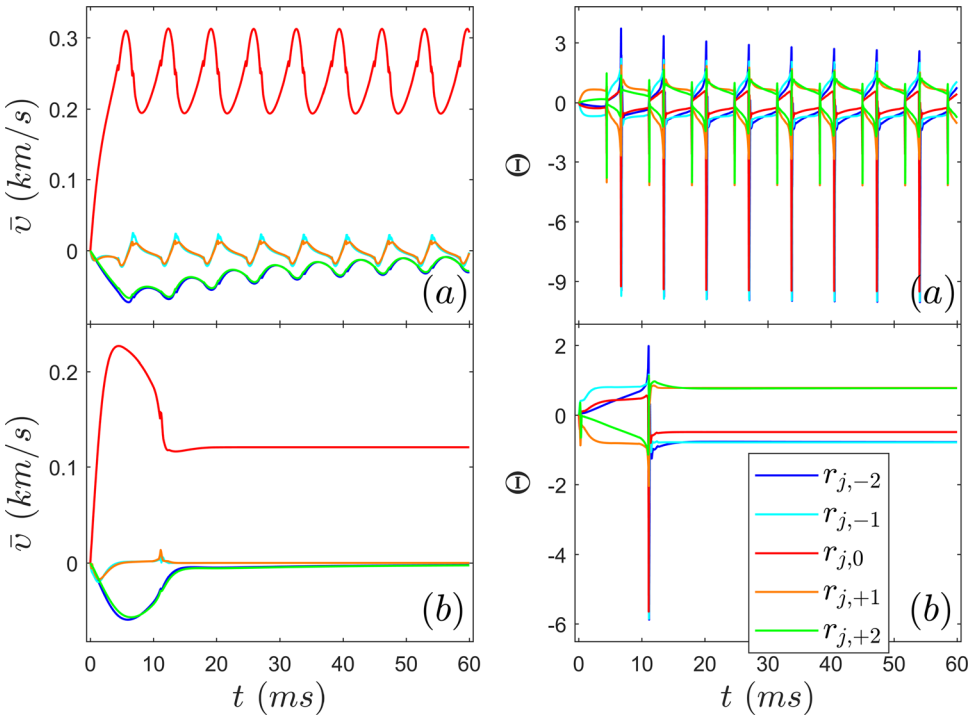

FIG. 5. The temporal process of zonal flow $\bar{v}(r,t)$ and phase function $\Theta(r,t)$ at five distinct spatial positions for (a) quasi-stationary and (b) stationary.

spikes of the phase function is further magnified in Fig. 7. One may notice the differences in the propagation characteristics; events 1 and 3 (2 and 4) propagate from left to right (right to left), strongly suggesting a pattern of wave energy propagation.

D. Blob-hole temporal structure triggered by zero-crossing of radial group velocity

The ITG wave energy under phase modulation is $I(r) \rightarrow I(r,t) = I(r)\cos^2(\Theta(r,t))$. The energy modulation factor $\cos^2(\Theta(r,t))$, calculated for the 15 ms interval of data for the phase function in Fig. 6 is displayed in Fig. 8. The portions, lasting several hundred μs, around four events at $r_{j,0}$ (further magnified in Fig. 9) exhibit the well-known blob-hole structure;[44,45] events 1 and 3 exhibit holes while events 2 and 4 exhibit blobs. The hole (temporal) structure is triggered by up zero-crossing of the radial group velocity; the down zero-crossing, on the other hand, triggers the blobs. Because the rapidity of up-zero-crossing is higher than that of down-zero-crossing in our calculation, the lifetime of holes is shorter than that of blobs.

E. Two phases of wave energy evolution: Caviton and Instanton

To describe the wave energy evolution, we will frequently use the terms Caviton as well as Instanton. These

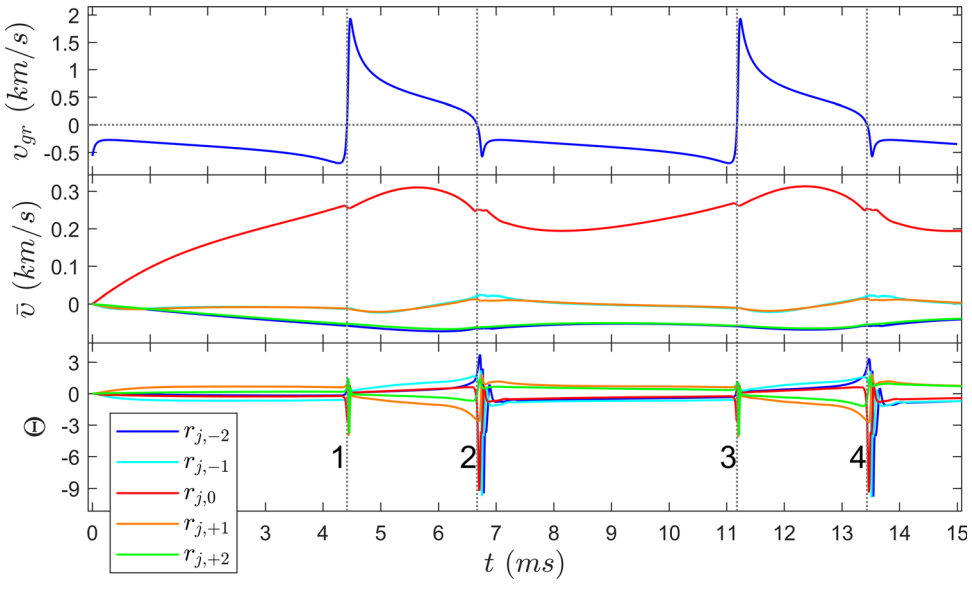

FIG. 6. The time evolution of first 15 ms for 5 distinct spatial positions to display the relationship of kinks, spikes, and zero-crossing of radial group velocity.

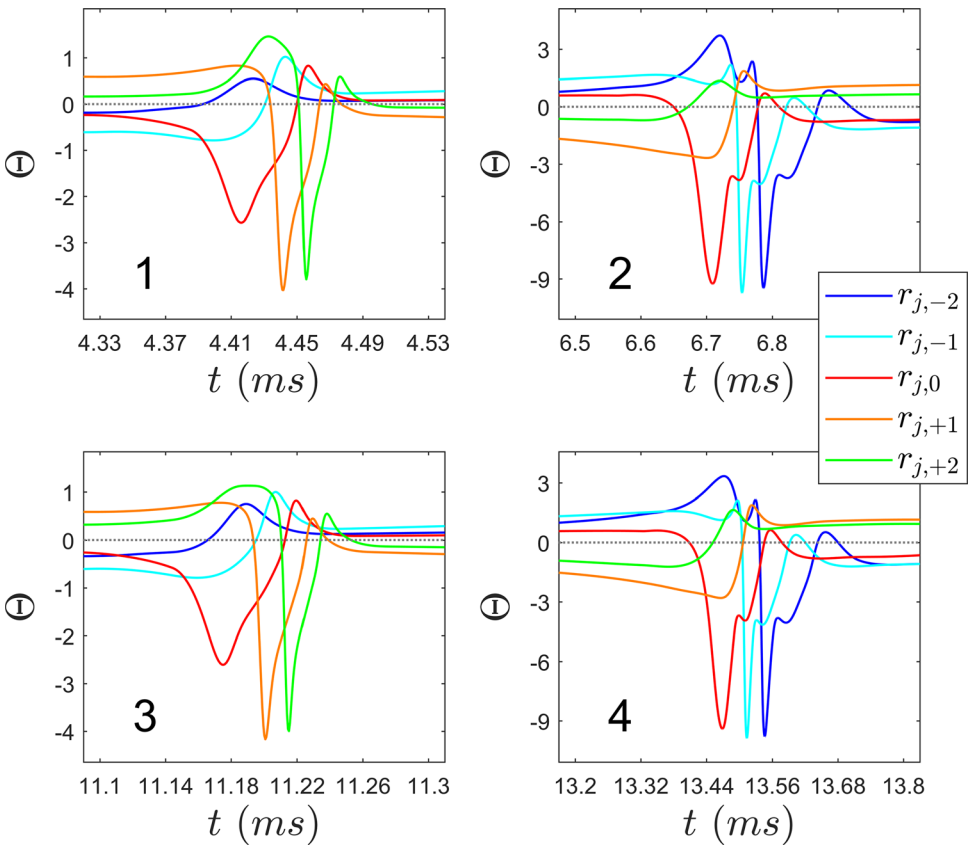

FIG. 7. Magnified portion near 4 spikes in Fig. 6.

terms used here have somewhat different meaning from their original. Specifically, in this paper, Caviton denotes a spatial region of (highly) reduced wave energy, and Instanton refers to a temporal localization in propagation of wave energy. Interested readers may find the original definitions in Refs. 46 and 47 for these two terms. Their selective snapshots for ITG wave energy are shown in Fig. 10.

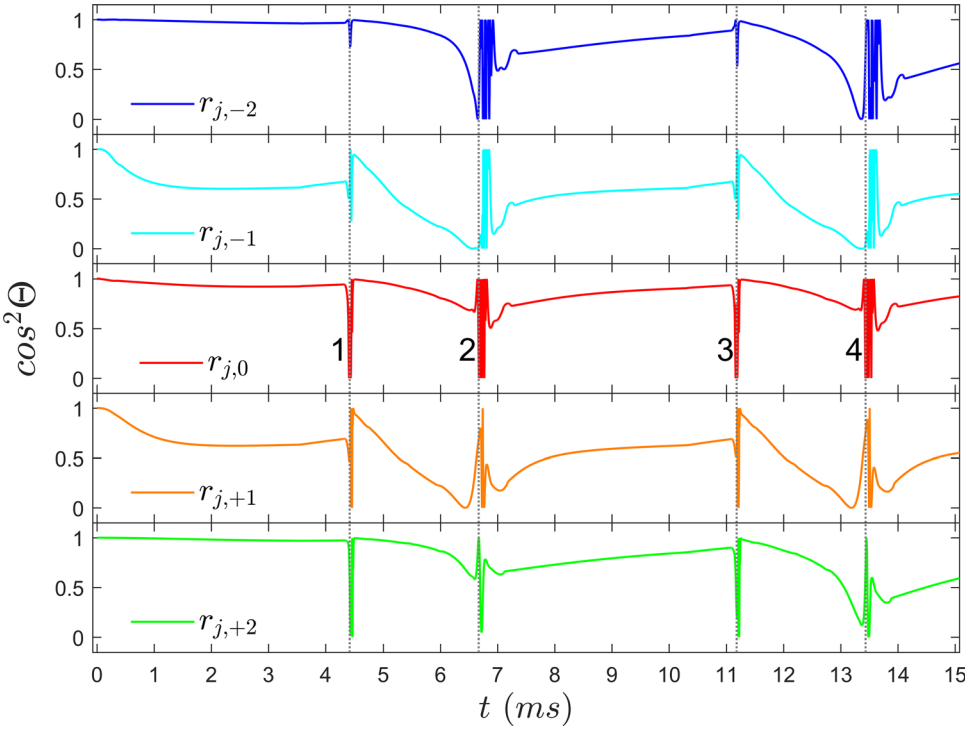

FIG. 8. The time evolution of drift wave amplitude $\cos^2\Theta$ of first 15 ms for 5 distinct spatial positions.

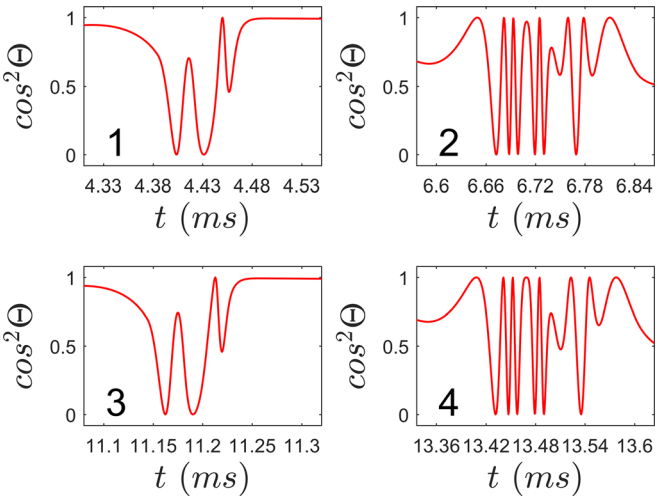

FIG. 9. Magnified portion near 4 spikes in Fig. 8.

The data in Secs. V A–V D, show-cased in the movie file in the caption of Fig. 10 (Multimedia view), reveal the pattern of wave energy evolution. Initially, a pair of Cavitons emerges at the dipole peak positions of the static Reynolds stress. They keep growing, breathing till $t_1 = 4.4$ ms, when suddenly the pair starts splitting into many Instantons that move, very rapidly, to the right before being absorbed at positive infinity (beyond the meso-scale). At little prior to that moment, a second pair of Cavitons emerges at the dipole peak positions, keeps growing, breathing till $t_2 = 6.7$ ms, when suddenly the pair splits into many Instantons, but this set moves, very rapidly, to the left getting absorbed at negative infinity. At sometime prior to that moment, a third Caviton pair forms at the dipole peak positions, keeps growing, breathing till $t_3 = 11.2$ ms, when suddenly the pair breaks into many instantons, moves rapidly to the right to be absorbed at positive infinity. Such a cycle occurs repeatedly. According to this description, each cycle consists of two phases. In the first phase, a pair of Cavitons is generated and grows slowly localized in the reaction region, no long range radial propagation of wave energy. The second phase kicks off when the pair suddenly decays (as if triggered by a particle $r_g(t,\tau) \equiv \int_\tau^t ds v_{gr}(\vartheta(s))$ entering into reaction region to break) into many Instantons, each with a much finer spatial structure. Unlike Cavitons that move slowly and locally, Instantons, with a fine radial structure, move towards infinity very rapidly, just as a carrier sending (negative) wave energy away. The lifetime of Instanton essentially depends on the rapidity of zero-crossing. Since rapidity is higher for up-zero-crossing (events 1 and 3) than for down-zero-crossing (events 2 and 4) as shown in Fig. 9, the lifetime of right-moving Instantons is shorter than that of left-moving ones. Noticeably, the lifetime of Instantons is about several hundred μs $\sim$ blob-hole life time discussed in Sec. V D. In other words, the temporal structure of blob-hole could be a discrete spatial representation for Instantons. This is consistent with the observation in Sec. V D that the lifetime of blob is longer than that of hole. In a sense, the measurements of blob-hole can provide information of Instantons. Now, one can see the following correlations: up-zero-crossing results in holes as a discrete spatial representation of right-moving Instantons; down-zero-crossing results in blobs as a discrete spatial representation of left-moving Instantons. Tentatively, for the data pertaining to the fluid model and parameters in this paper, lifetime of holes and right-moving Instantons is shorter than that of blobs and left-moving Instantons.

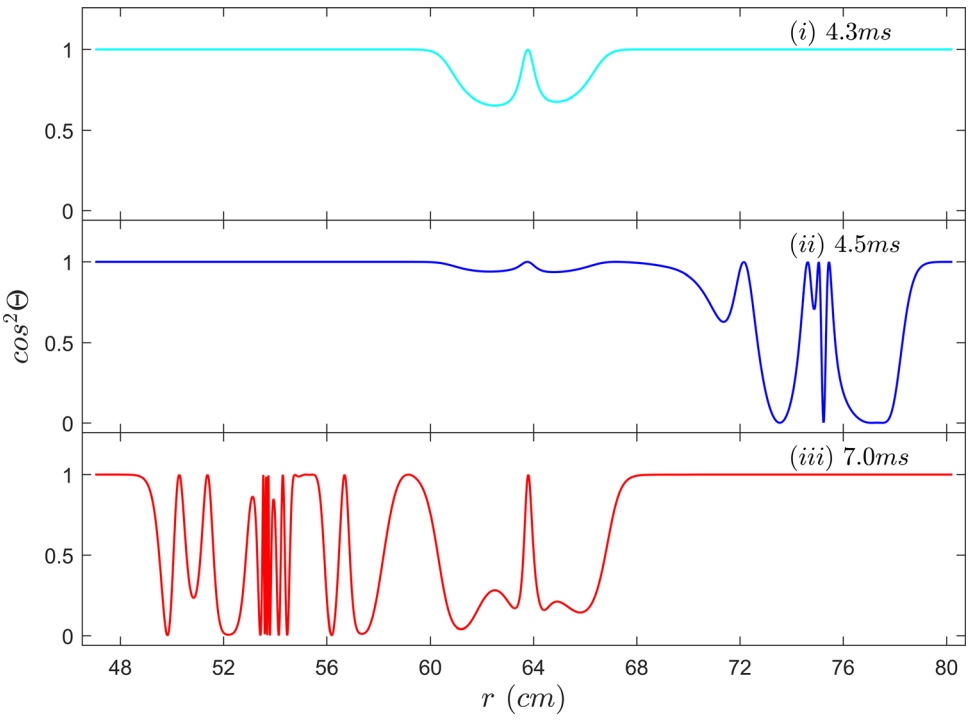

FIG. 10. The snapshots of caviton and instantons: (i) caviton, (ii) right-moving instantons, and (iii) left-moving instantons. The time evolution for first 15 ms can be seen via the link wave energy evolution. Multimedia view: https://doi.org/10.1063/1.4995302.2

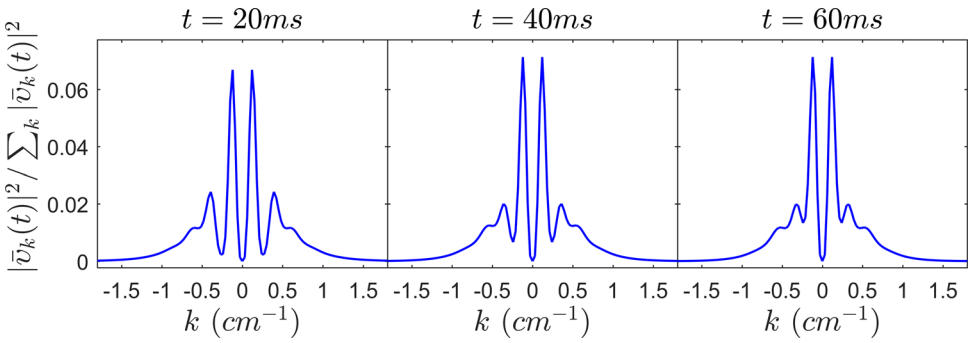

FIG. 11. The wave number spectrum of zonal flow at three distinct time points at $t = 20, 40, 60$ ms for quasi-stationary.

VI. NUMERICAL RESULTS IN FOURIER SPACE

Because spectral methods are widely used in experiments, we transform the last section's data for the quasi-stationary process into Fourier space. It also tells what would appear in Fourier representation for the local traveling wave.

A. Zonal flow wave-number spectrum at three time points

The spatial Fourier transform of $\bar{v}(r,t)$ (Fig. 4) at three distinct time points $t = 20, 40, 60$ ms is shown in Fig. 11. A pair of two-peak (leading and sub-leading) structures exhibits its symmetry in k-inversion. The leading (sub-leading) peak position at 0.13cm^{-1} ($0.40\ \text{cm}^{-1}$) is found to be growing (damping) for the following 40 ms, indicating a condensation in k-space. Alternatively, one may imagine that two pairs of quasi-particles of zonal flow are formed initially. The higher momentum quasi-particle transfers its intensity to lower momentum quasi-particle.

It is clearly seen that the leading portion of the local traveling wave is on the centimeter length scale, much longer than that of ITG drift waves.

B. Zonal frequency spectrum at five spatial points

In Fig. 12, the frequency spectra of $\bar{v}(r,t)$ at five distinct spatial positions are presented. It is remarkable to observe that the central peak of zero frequency disappears at $r_{j,\pm1}$. It could be blamed on the hot spot of breathing activities in these two areas.

C. Frequency wavenumber spectrum

Generally speaking, such a spectrum could be viewed as a coarse-grained dispersion relation if the frequency wavenumber relationship was a diffuse (rather than a conventional sharp) curve. Instead, such "broaden curves" in Fig. 13 appear to be composed of several separated step functions, suggesting a kind of continuum for distinct wave numbers with evanescent intensity from zero frequency. Here, continuum refers to such a feature that the frequency is essentially independent of wave number.

D. Pseudo eigenmode

The small oscillation in the quasi-stationary process is found to be related to a pseudo eigenmode in the power spectrum as shown in Fig. 14. Such phenomena have been reported in the literature.[34,36] For the quasi-stationary process, there is a peak at 0.15 kHz, which matches the oscillation shown in Fig. 6 with the period close to 6.7 ms as dictated by the period of radial group velocity.

E. Lissajous diagram

The Lissajous diagram for the phase relationship of zonal flow with turbulence amplitude variation has been widely studied in the so-called i-phase of L-H transition,[34,35] primarily in order to check the causality of prey-predator model, which is a (zero spatial) temporal model. In this model there are only two choices, denoted by J-Y,[34] when one is prey, the other can only be a predator. In Fig. 15, the time variation of turbulence amplitude is represented by $\cos\Theta$. The results indicate that the choice of J-Y is dependent on the radial position.

VII. NONLINEAR COUPLING BETWEEN MULTIPLE RATIONAL SURFACES VIA ZONAL FLOW

In this section, we present preliminary results from nonlinear coupling between multiple rational surfaces via zonal flow. The word "preliminary" means that only a few

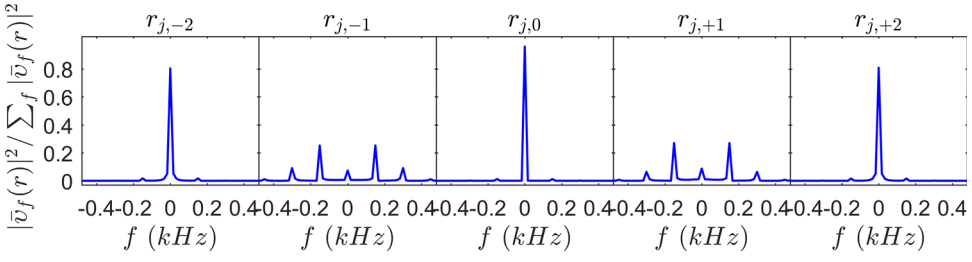

FIG. 12. The frequency spectrum of zonal flow $\bar{v}(r,t)$ at five distinct spatial positions for quasi-stationary.

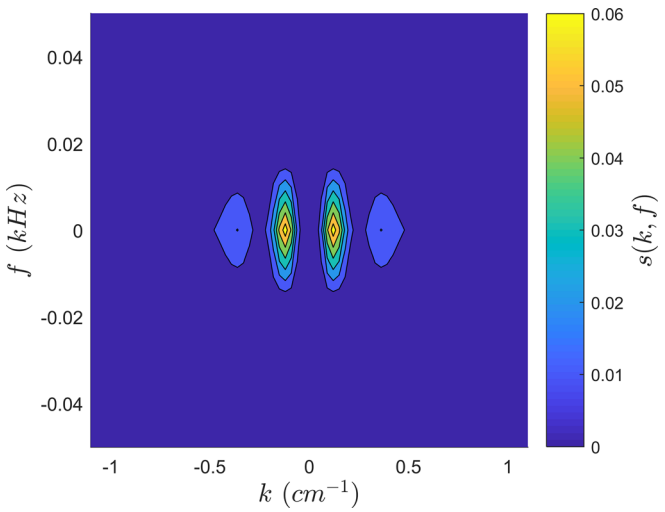

FIG. 13. The frequency wave number spectrum of zonal flow $\bar{v}(r,t)$ for quasi-stationary.

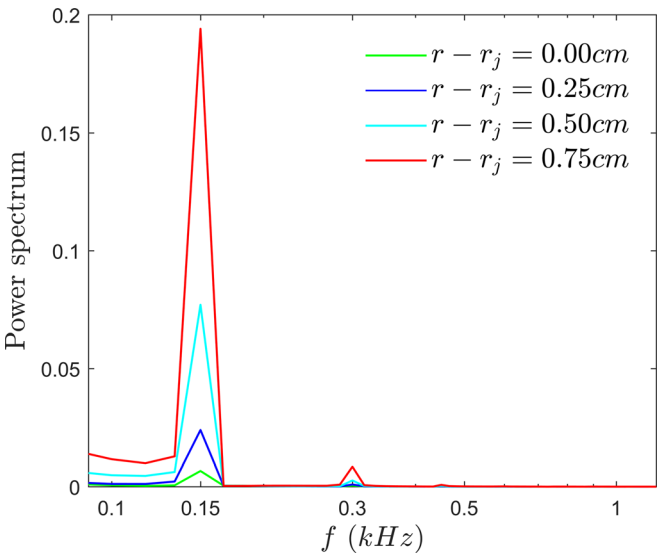

FIG. 14. The frequency spectrum of zonal flow $\bar{v}(r,t)$ for quasi-stationary at four distinct spatial positions.

selective samples are chosen under simplified assumptions like: (1) no variation of equilibrium parameters throughout the chosen rational surfaces is allowed; (2) the initial randomness of excitation among individual rational surfaces is ignored; and (3) artificial truncation of the chain of coupled rational surfaces is introduced.

In tokamaks, the linear eigenmodes localized at various rational surfaces are independent. The independence could reflect in the excitation time for the ITG mode associated with a given rational surface. For a given rational surface r_j, the ITG mode is destabilized at t_j, while for $r_{j\pm1}$ at $t_{j\pm1}$ where t_j and $t_{j\pm1}$ are statistically independent within an e-folding interval of inverse growth rate γ. Since each linear mode at a given rational surface has a radial extension $\approx\sqrt{n\sigma}$ [see Eq. (18)], much broader than the distance between neighboring rational surfaces: $\Delta x = 1$, there is a significant overlap between the modes pertaining, for instance, to r_0 and to $r_{\pm1}$. In other words, the reaction term in Reynolds stress at x arises not only from the rational surface at r_0 but also from multiple rational surfaces located at r_0, $r_{\pm1}$, $r_{\pm2}$, …, $r_{\pm j_{max}}$. Since the emphasis of the present theory is to expose the interplay between micro and meso scales, we will affect a truncation of $j_{max} = 15$ (within a range of 10 cm). The zonal flow equation, in which coupling among 31 rational surfaces is included, comes out to be

$$\frac{\partial V(x,t)}{\partial t} + \frac{\partial}{\partial x}\left[\sum_{j=-j_{max}}^{j_{max}} R_j(x)\cos^2\left(\Theta_j(x,t)\right)\right] - \frac{1}{R_z}\frac{\partial^2 V(x,t)}{\partial x^2} + \gamma_F V(x,t) = 0 \tag{24}$$

with the phase function of each rational surface under influence by the same zonal flow

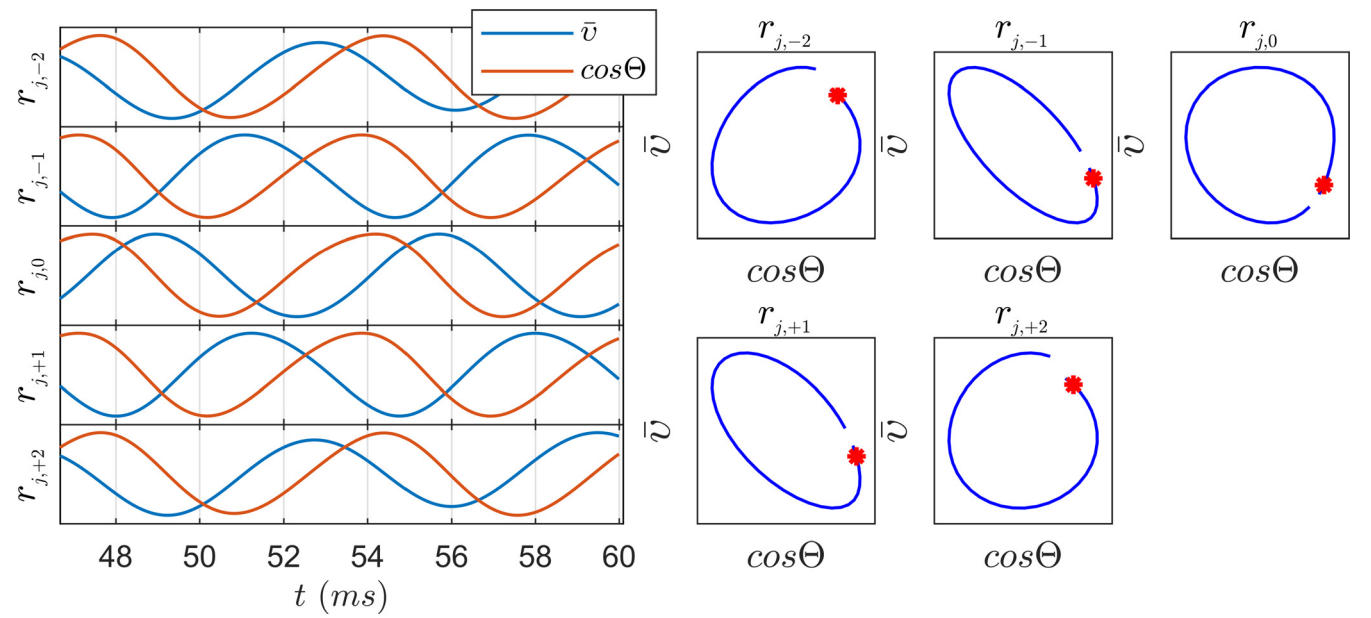

FIG. 15. Lissajous diagram of zonal flow $\bar{v}(r,t)$ versus amplitude of fluctuation modulated by zonal flow at five distinct spatial positions for quasi-stationary.

$$\Theta_j(x,\tau) = \int_{\tau_{j0}}^{\tau} d\tau' V\left(x + j - \hat{s}\int_{\tau'}^{\tau} d\sigma \hat{v}_{gr}(\vartheta(\sigma)), \tau'\right), \quad (25)$$

where τ_{j0} stands for the time when the ITG mode associated with r_j is destabilized. It is reasonable to assume that $\gamma\tau_{j0}$ is a random number in $[0, 1]$. To simplify our presentation, we make the additional assumption $\tau_{j0} = 0$ for $|j| \le j_{\max}$, quite adequate for the fast growing ITG mode, because the variation of τ_{j0} is very small compared to the initial growth time of the zonal flow. In the present paper, the effects from shear flow suppression[48–50] have not been taken into account. The last term of Eq. (24), $\gamma_F V(x,t)$, is introduced to stand for the back reaction from poloidal rotation driven by zonal flow, as adopted in Eq. (2.4) of Ref. 7. The zonal flow-ITG wave system is NOT a closed system, because zonal flow drives poloidal rotation, which in turn is dissipated by magnetic pumping or by transferring the motion away in some other forms. γ_F could also be a function of position and time; however, it is assumed to be a suitable constant in this paper corresponding to 50 Hz in physical unit. For later convenience, a new set of symbols $\bar{r}_j \equiv r_j + x_0/\hat{s}k_\vartheta$ is introduced to label the radial position of the Reynolds stress center associated with the rational surface r_j, where x_0 is the dimensionless shift of Reynolds stress center away from the rational surface as defined by Eq. (17).

We will now numerically solve Eqs. (24) and (25) for up to a time span of 60 ms by setting left (right) end truncation at $\bar{r}_{-15}$ =58.9 cm ($\bar{r}_{15}$=68.3 cm) and by making use of a simple ITG turbulence profile model near plasma edge: (a) The plasma edge is assumed at 68.5 cm, (b) Turbulence level falls off from full value at $\bar{r}_{10}$(66.8 cm) to zero at $\bar{r}_{15}$ (68.3 cm) linearly, and (c) Turbulence level falls off from full value at $\bar{r}_{-4}$ (62.4 cm) to zero at $\bar{r}_{-15}$ (58.9 cm) linearly. For the quasi-stationary process, the calculated zonal flow values are displayed in Fig. 16. The solid curves correspond to three different times: 20 ms (cyan), 40 ms (blue), and 60 ms (red). However, one can readily see a problem; the zonal flow extends outside the plasma edge. In order to avoid complicated edge physics, we just simply draw an artificial interpolated black dot line between 68.5 cm and the zero-crossing point, adopting the same radial position at minimum zonal flow at 68.1 cm. The spatial period of the fine oscillatory structure can be seen to be 0.3 cm, which is very close to the distance between adjacent rational surfaces. Since the zonal flow and electric field have opposite signs (per our coordinate convention), the profile in Fig. 16 looks very similar to the pattern observed in the JET Ohmic phase[51] at most positions except for an asymmetric dipole structure at left end (outside the data domain). This structure emerges because of a drive originating in the gradient of the turbulence level. The magnitude of the dip, in fact, measures the attenuation rate of ITG turbulence towards the plasma center. It is thus very desirable to see any evidence from experiments regarding existence of such a *seed* interior shear flow.

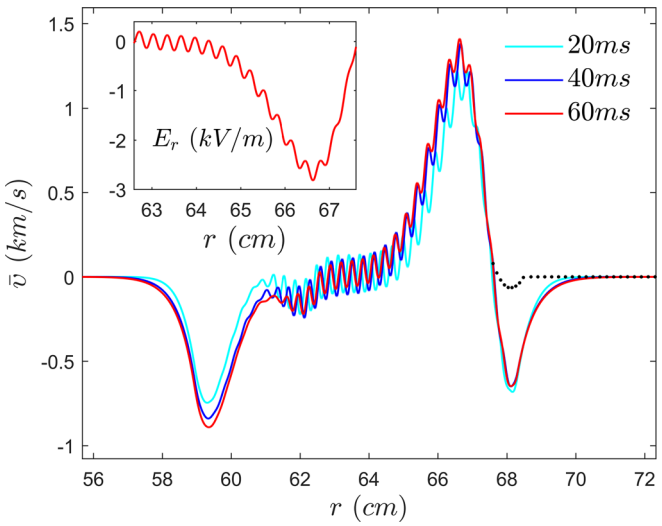

FIG. 16. The spatial structure of zonal flow $\bar{v}(r,t)$ of 31 rational surfaces at three distinct time points at $t = 20, 40, 60$ ms for the quasi-stationary process.

For the stationary process, the radial profiles of zonal flow are essentially the same as those displayed in Fig. 16.

VIII. SUMMARY AND DISCUSSIONS

A. Reynolds stress and group velocities in tokamak

Two basic elements of the zonal flow theory used in this paper are ITG linear equation set, Eqs. (1)–(3), [38] and the zonal flow equation derived as the surface averaged nonlinear vorticity equation,[39] Eqs. (13) and (14); both follow from Braginskii's fluid model. This well-known model was used to calculate, at least qualitatively correctly, the Reynolds stress and group velocities in the context of ITG turbulence in tokamaks. For this purpose, we invoked a carefully calculated analytical expression of the ITG eigenmode in Fourier-ballooning representation.[32,33] The Reynolds stress has the structure of a dipole with a small monopole contribution. The group velocities are only the function of poloidal coordinate, because the ITG eigenmode in tokamak is a standing wave in the radial direction. The poloidal group velocity plays the role of mapping poloidal angle to time. The radial group velocity is found to be a zero-crossing periodic function in time composed of two sharp edges with two smooth phases in between.

B. Caviton and instanton behind blob-hole

As long as radial group velocity remains in the smooth phase, the ITG wave energy moves like a pair of "breathing" Cavitons. Zero-crossing of radial group velocity, which occurs only at a sharp edge, triggers Cavitons to decay into many Instantons. The ways of zero-crossing of radial group velocity at a sharp edge determine the Instanton signature—formation of a blob or a hole. Up-zero-crossing results in holes (right-moving instantons) and Down-zero-crossing results in blobs (left-moving instantons). The rapidity of zero-crossing determines the lifetime of blob-hole, which is a discrete spatial representation of Instantons.

C. Identifying theoretical constructs with experimental observations

Some spatiotemporal features difficult for diagnostics in real space could be recognized by its counterpart in Fourier space, e.g., the pseudo eigenmodes describe period of a quasi-

stationary process; separated continuum in the frequency wavenumber spectrum describes a local traveling wave.

In addition to the equilibrium parameters, there are quite a few other significant parameters that define the RDA equation set that models the ITG-Zonal Flow system, for example, the ITG mode frequency and η^2 for mode structure, the cutoff distance for Instantons ($x_{+\infty} - x_{-\infty}$), and the number of rational surfaces in nonlinear coupling via zonal flow ($2j_{\max} + 1$). Interestingly, some of these parameters are, in principle, identifiable in experiment:

(1) By measuring non-linear frequency shift (the so-called correlation shift) as well as frequency broadening,[52] one could deduce both the mode frequency and specific information for the mode structure.
(2) The cutoff distance for Instantons can be deduced from the lifetime of blob-hole measured in experiments. It may provide information for verifying likelihood of various cutoff mechanisms such as Anderson localization.[53,54] $j_{\max}$ could also be experimentally determined when a scheme of diagnostics like Doppler backscattering (DBS) is able to extend further inside plasma.

D. Conclusion and beyond

The new findings of this paper in zonal flow physics are summarized as follows:

- Zonal flow is found to grow with pure phase modulation and saturates in a range of km/s for JET like low mode parameters (without a linear instability).
- Stationary and quasi-stationary zonal flows, sharing similar spatial attributes, have a quadrupole structure near a single rational surface. The stationary process arises whenever poloidal group velocity comes to a zero-crossing and gets stuck there. The temporal structures of the two processes, however, are very different (also true for multiple surface coupling).
- The quasi-stationary process is characterized by a period equal to the period of the radial group velocity. In the auto spectrum, it appears to be a pseudo eigenmode in the kHz range.
- The zonal flow is a local traveling wave without long-range propagation. In Fourier (k) space, it is shown to consist of two peaks at plus/minus k.
- The temporal pattern of radial group velocity has a significant impact on the propagation of ITG wave energy. For the quasi-stationary process, the periodic radial group velocity is composed of two sharp edges and two smooth phases in between. The zero-crossing of radial group velocity occurs only in sharp phases.
- Two distinct spatiotemporal structures follow. Most of the time, one sees a pair of Cavitons without long range propagation. Upon zero crossing, Caviton pair decays into many Instantons propagating rapidly into infinity.
- The discrete spatial representation of Instantons is highly correlated with the so-called Blob-Hole temporal structures observed in experiments. Right (left) moving Instanton corresponds to Holes (Blobs). Their lifetime is in a range of hundred μs.
- The radial profile contributed from 31 nonlinearly coupled rational surfaces (near plasma edge) looks very similar to the observations in the JET Ohmic phase[51] for both stationary and quasi-stationary processes.
- The theory predicts an interior asymmetric dipole structure of zonal flow driven by gradients of the ITG turbulence level (a ponderomotive force). Such a structure occurs in the region outside the observation region in the JET Ohmic phase.[51] Further analysis of JET data could test this prediction.

The results of this theory, based on the Braginskii fluid model, can be reproduced in a theory based on the gyrokinetic model. We expect that major qualitative features would be retained. In a recently constructed linear kinetic model for ITG,[55] the analytical expression of the ITG eigenmode is essentially the same as used in this paper [Eq. (16)]. Kinetic modifications are likely to be only quantitative. It is noticeable that the use of kinetic theory to calculate Reynolds stress has been performed by Qiu, Chen, and Zonca.[56]

In general, the group velocities could be singular. As a result, the ITG wave energy modulation is no longer restricted to pure phase modulation. This scenario will be explored in future.

ACKNOWLEDGMENTS

Two of the authors (Y. Z. Zhang and Z. Y. Liu) are grateful to Professor A. D. Liu and Dr. D. F. Kong for discussions on the related experimental data and also to Professor H. Berk for helpful discussions and encouragements. This research was supported by the Key Research Program of Frontier Sciences CAS (No. QYZDB-SSWSYS004), National Magnetic Confinement Fusion Energy Research Project (No. 2015GB111003), National Natural Science Foundation of China (Nos. NSFC-11575185 and 11575186), Scientific Research Fund of the Sichuan Provincial Education Department Grant No. 17ZA0281, Foundation of Sichuan University of Science and Engineering Grant No. 2016RCL21, and the U.S. Dept. of Energy Grant No. DE-FG02-04ER-54742.

APPENDIX A: CALCULATING AVERAGE OF THREE OPERATORS OVER FAST SCALE

Throughout this appendix, the tilt over fast variable is dropped. The average of three operators in the group velocities is defined under Eq. (11). Explicitly, they are

$$\langle \mathrm{K}_r \rangle \equiv \frac{\int dr \hat{\varphi}^* (-i\partial_r \hat{\varphi})}{\int dr \hat{\varphi}^* \hat{\varphi}}, \quad \langle \mathrm{K}_r^2 \rangle \equiv \frac{\int dr \hat{\varphi}^* \left(-\partial_r^2 \hat{\varphi}\right)}{\int dr \hat{\varphi}^* \hat{\varphi}}, \quad \langle \nabla_\parallel^2 \rangle \equiv \frac{\int dr \hat{\varphi}^* \left(\nabla_\parallel^2 \hat{\varphi}\right)}{\int dr \hat{\varphi}^* \hat{\varphi}}. \tag{A1}$$

For the chosen representation $\hat{\varphi}(r, \vartheta, \zeta) \equiv \exp(in\zeta - im\vartheta) \sum_l \varphi_l(r) \exp(-il\vartheta) \equiv \exp(in\zeta)\hat{\varphi}_n(r, \vartheta)$ use is made of the 2D ballooning wave function Eq. (16) to obtain the 2D ITG wave function in $x - l$ representation[33]

$$\hat{\varphi}_n(r,\vartheta) \sim \sum_l \exp\left[ik_*(\lambda_*)(x-l) - \frac{i(x-l)^2}{2\eta^2}\right] \times \exp\left[-\frac{l^2}{2n\beta_2} - il\left(\vartheta + i\frac{\beta_1}{\beta_2}\right)\right]. \quad \text{(A2)}$$

This form makes it easy to get the action of operators on the wave functions. The common factor outside the summation over l has been ignored because of cancellation in the average. Explicitly

$$-i\partial_r\hat{\varphi}_n(r,\vartheta) \sim k_\vartheta\hat{s}\sum_l\left[k_*(\lambda_*) - \frac{(x-l)}{\eta^2}\right] \times \exp\left[ik_*(\lambda_*)(x-l) - \frac{i(x-l)^2}{2\eta^2}\right] \times \exp\left[-\frac{l^2}{2n\beta_2} - il\left(\vartheta + i\frac{\beta_1}{\beta_2}\right)\right], \quad \text{(A3)}$$

$$-\partial_r^2\hat{\varphi}_n(r,\vartheta) \sim (k_\vartheta\hat{s})^2\sum_l\left[\frac{i}{\eta^2} + \left(k_*(\lambda_*) - \frac{(x-l)}{\eta^2}\right)^2\right] \times \exp\left[ik_*(\lambda_*)(x-l) - \frac{i(x-l)^2}{2\eta^2}\right] \times \exp\left[-\frac{l^2}{2n\beta_2} - il\left(\vartheta + i\frac{\beta_1}{\beta_2}\right)\right], \quad \text{(A4)}$$

$$\nabla_\parallel^2\hat{\varphi}_n(r,\vartheta) \sim -\frac{1}{(qR)^2}\sum_l (x-l)^2 \times \exp\left[ik_*(\lambda_*)(x-l) - \frac{i(x-l)^2}{2\eta^2}\right] \times \exp\left[-\frac{l^2}{2n\beta_2} - il\left(\vartheta + i\frac{\beta_1}{\beta_2}\right)\right]. \quad \text{(A5)}$$

Then, the ϑ dependences of $\langle K_r\rangle$, $\langle K_r^2\rangle$, and $\langle\nabla_\parallel^2\rangle$ are then obtained numerically based on Eqs. (A3)–(A5).

APPENDIX B: DIFFUSIVE BOUNDARY CONDITION FOR THE ZONAL FLOW EQUATION

The zonal flow equation Eq. (20) reduces to the diffusive equation where Reynolds stress is small,

$$\frac{\partial V(x,\tau)}{\partial\tau} = \frac{1}{R_z}\frac{\partial^2 V(x,\tau)}{\partial x^2}. \quad \text{(B1)}$$

The zonal flow obtained analytically is shown below,

$$V(x,\tau) = \int_0^\tau V(x_r,\sigma)\frac{\sqrt{R_z}(x-x_r)}{2\sqrt{\pi(\tau-\sigma)^3}} \times \exp\left[-\frac{R_z(x-x_r)^2}{4(\tau-\sigma)}\right]d\sigma, \quad x \ge x_r, \quad \text{(B2)}$$

$$V(x,\tau) = \int_0^\tau V(x_l,\sigma)\frac{\sqrt{R_z}(x_l-x)}{2\sqrt{\pi(\tau-\sigma)^3}} \times \exp\left[-\frac{R_z(x_l-x)^2}{4(\tau-\sigma)}\right]d\sigma, \quad x \le x_l, \quad \text{(B3)}$$

where $x_r \equiv x_0 + 4\sqrt{n\sigma}x_l \equiv x_0 - 4\sqrt{n\sigma}$.

APPENDIX C: SOLUTION OF THE PHASE FUNCTION BY DIRECT INTEGRATION

Use is made of Eq. (22) to compute the phase function

$$\Theta(x,\tau) = \int_0^\tau d\tau' V\left(x - \hat{s}\int_{\tau'}^\tau d\sigma\hat{v}_{gr}(\vartheta(\sigma)),\tau'\right). \quad \text{(C1)}$$

We now seek for an approach to calculate

$$\Theta(x,\tau+\Delta\tau) = \int_0^{\tau+\Delta\tau} d\tau' V\left(x - \hat{s}\int_{\tau'}^{\tau+\Delta\tau} d\sigma\hat{v}_{gr}(\vartheta(\sigma)),\tau'\right) \quad \text{(C2)}$$

in order to utilize $\Theta(x,\tau)$ without doing integration before τ.

Splitting the r.h.s of Eq. (C2) into two terms

$$\Theta(x,\tau+\Delta\tau) = \int_0^{\tau} d\tau' V\left(x - \hat{s}\int_{\tau'}^{\tau+\Delta\tau} d\sigma\hat{v}_{gr}(\vartheta(\sigma)),\tau'\right) + \int_\tau^{\tau+\Delta\tau} d\tau' V\left(x - \hat{s}\int_{\tau'}^{\tau+\Delta\tau} d\sigma\hat{v}_{gr}(\vartheta(\sigma)),\tau'\right), \quad \text{(C3)}$$

one can readily see that that the first term is $\Theta(x-\Delta x_1,\tau)$, where $\Delta x_1 = \hat{s}\int_\tau^{\tau+\Delta\tau} d\sigma\hat{v}_{gr}(\vartheta(\sigma))$. Now we have

$$\Theta(x,\tau+\Delta\tau) = \Theta(x-\Delta x_1,\tau) + \int_\tau^{\tau+\Delta\tau} d\tau' V(x-\Delta x_2,\tau'), \quad \text{(C4)}$$

where $\Delta x_2 \equiv \hat{s}\int_{\tau'}^{\tau+\Delta\tau} d\sigma\hat{v}_{gr}(\vartheta(\sigma))$ for $\tau' \ge \tau$.

Since $\hat{v}_{gr}(\vartheta(\sigma))$ is a known function, Δx_2 can be stored as a 2D matrix. However, $x-\Delta x_1$ and $x-\Delta x_2$ generally do not fall on the grid point precisely. A special numerical skill, e.g., Lagrangian interpolation up to fourth order, has been devised and implemented.

APPENDIX D: SOLUTION OF PHASE FUNCTION BY FAST FOURIER TRANSFORM

The differential form of the phase function as expressed by Eq. (22) is

$$\frac{\partial\Theta(x,\tau)}{\partial\tau} + \hat{s}\hat{v}_{gr}(\tau)\frac{\partial\Theta(x,\tau)}{\partial x} = V(x,\tau). \quad \text{(D1)}$$

Use is made of the spatial Fourier transform to convert Eq. (D1) into Fourier form with the periodic boundary condition $\Theta(x_{\pm\infty},\tau) = 0$ (as mentioned at the end of Sec. V A, the precise position of $x_{\pm\infty}$ has little impact on the final results),

$$\frac{d\Theta_p(\tau)}{d\tau} + ip\hat{s}\hat{v}_{gr}(\tau)\Theta_p(\tau) = V_p(\tau). \tag{D2}$$

The analytical solution is

$$\Theta_p(\tau) = \int_0^\tau d\tau' V_p(\tau') \exp\left[-ip\hat{s}\int_{\tau'}^\tau d\sigma \hat{v}_{gr}(\vartheta(\sigma))\right]. \tag{D3}$$

[1]G. W. Hammett, M. A. Beer, W. Dorland, S. C. Cowley, and S. A. Smith, Plasma Phys. Controlled Fusion **35**, 973 (1993).
[2]A. M. Dimits, T. J. Williams, J. A. Byers, and B. I. Cohen, Phys. Rev. Lett. **77**, 71 (1996).
[3]A. Hasegawa and M. Wakatani, Phys. Rev. Lett. **59**, 1581 (1987).
[4]Z. Lin, T. S. Hahm, W. W. Lee, W. M. Tang, and R. B. White, Science **281**, 1835 (1998).
[5]P. H. Diamond, S.-I. Itoh, K. Itoh, and T. S. Hahm, Plasma Phys. Controlled Fusion **47**, R35 (2005).
[6]K. Itoh, S.-I. Itoh, and P. H. Diamond, Phys. Plasmas **13**, 055502 (2006).
[7]A. Fujisawa, Nucl. Fusion **49**, 013001 (2009).
[8]Z. Lin, T. S. Hahm, W. W. Lee, W. M. Tang, and P. H. Diamond, Phys. Rev. Lett. **83**, 3645 (1999).
[9]A. I. Smolyakov and P. H. Diamond, Phys. Plasmas **6**, 4410 (1999).
[10]A. I. Smolyakov, P. H. Diamond, and V. I. Shevchenko, Phys. Plasmas **7**, 1349 (2000).
[11]L. Chen, Z. Lin, and R. B. White, Phys. Plasmas **7**, 3129 (2000).
[12]P. N. Guzdar, R. G. Kleva, A. Das, and P. K. Kaw, Phys. Rev. Lett. **87**, 015001 (2001).
[13]P. N. Guzdar, R. G. Kleva, and L. Chen, Phys. Plasmas **8**, 459 (2001).
[14]S. Champeaux and P. H. Diamond, Phys. Lett. A **288**, 214 (2001).
[15]G. Manfredi, C. M. Roach, and R. O. Density, Plasma Phys. Controlled Fusion **43**, 825–1001 (2001).
[16]K. Hallatschek and P. H. Diamond, New J. Phys. **5**, 29 (2003).
[17]L. Chen, R. B. White, and F. Zonca, Phys. Rev. Lett. **92**, 075004 (2004).
[18]F. Zonca, L. Chen, and R. B. White, Phys. Plasmas **11**, 2488 (2004).
[19]Z. Lin, L. Chen, and F. Zonca, Phys. Plasmas **12**, 056125 (2005).
[20]J. Anderson, H. Nordman, R. Singh, and J. Weiland, Plasma Phys. Controlled Fusion **48**, 651 (2006).
[21]A. B. Mikhailovskii, A. I. Smolyakov, E. A. Kovalishen, M. S. Shirokov, V. S. Tsypin, and R. M. O. Galvão, Phys. Plasmas **13**, 052516 (2006).
[22]O. D. Gurcan and P. H. Diamond, J. Phys. A: Math. Theor. **48**, 293001 (2015).
[23]Z. B. Guo and T. S. Hahm, Nucl. Fusion **56**, 066014 (2016).
[24]M. N. Rosenbluth and F. L. Hinton, Phys. Rev. Lett. **80**, 724 (1998).
[25]F. L. Hinton and M. N. Rosenbluth, Plasma Phys. Controlled Fusion **41**, A653 (1999).
[26]R. S. Johnson, *Singular Perturbation Theory* (Springer, New York, 2005), Chap. 4.
[27]J. W. Connor, R. J. Hastie, and J. B. Taylor, Phys. Rev. Lett. **40**, 396 (1978).
[28]Y. C. Lee and J. W. Van Dam, in *Proceedings of the Finite Beta Theory Workshop*, Varenna Summer School of Plasma Physics, September 1977, Varenna, Italy, edited by B. Coppi and B. Sadowski (U.S. Department of Energy, Office of Fusion Energy, Washington DC, 1979), Paper No. CONF-7709167, p. 93.
[29]J. W. Connor, R. J. Hastie, and J. B. Taylor, Proc. R. Soc. London, Ser. A **365**, 1 (1979).
[30]Y. Z. Zhang and S. M. Mahajan, Phys. Plasmas **2**, 4236 (1995).
[31]Y. Z. Zhang and S. M. Mahajan, Phys. Lett. A **157**, 133 (1991).
[32]T. Xie, H. Qin, Y. Z. Zhang, and S. M. Mahajan, Phys. Plasmas **23**, 042514 (2016).
[33]T. Xie, Y. Z. Zhang, S. M. Mahajan, Z. Y. Liu, and H. He, Phys. Plasmas **23**, 102313 (2016).
[34]J. Cheng, J. Q. Dong, K. Itoh, L. W. Yan, M. Xu, K. J. Zhao, W. Y. Hong, Z. H. Huang, X. Q. Ji, W. L. Zhong *et al.*, Phys. Rev. Lett. **110**, 265002 (2013).
[35]L. Schmitz, L. Zeng, T. L. Rhodes, J. C. Hillesheim, W. A. Peebles, R. J. Groebner, K. H. Burrell, G. R. McKee, Z. Yan, G. R. Tynan *et al.*, Nucl. Fusion **54**, 073012 (2014).
[36]D. F. Kong, T. Lan, A. Liu, L. W. Yan, H. L. Zhao, H. G. Sheng, R. Chen, J. L. Xie, H. Li, W. D. Liu, C. X. Yu *et al.*, "The evolution of the mean flow and zonal flow during the L-I-L transitions on HL-2A," in Proceedings of the EPS Meeting, Helsinki (2013), p. P2.171.
[37]G. S. Xu, H. Q. Wang, M. Xu, B. N. Wan, H. Y. Guo, P. H. Diamond, G. R. Tynan, R. Chen, N. Yan, D. F. Kong, H. L. Zhao, A. D. Liu, T. Lan *et al.*, Nucl. Fusion **54**, 103002 (2014).
[38]W. Horton, R. D. Estes, and D. Biskamp, Plasma Phys. **22**, 663 (1980).
[39]M. Wakatani and A. Hasegawa, Phys. Fluids **27**, 611 (1984).
[40]T. Xie, Y. Z. Zhang, S. M. Mahajan, and A. K. Wang, Phys. Plasmas **19**, 072105 (2012).
[41]G. Nicolis and I. Prigogine, *Self-Organization in Non Equilibrium Systems* (Wiley, New York, 1977).
[42]H. Haken, *Synergetics, Introduction and Advanced Topics* (Springer, Berlin, 2004).
[43]W. H. Press, S. A. Teukolsky, W. T. Vetterling, and B. P. Flannery, *Numerical Recipes-The Art of Scientific Computing*, 3rd ed. (Cambridge, New York, 2007).
[44]G. S. Xu, V. Naulin, W. Fundamenski, C. Hidalgo, J. A. Alonso, C. Silva, B. Goncalves, A. H. Nielsen, J. J. Rasmussen, S. I. Krasheninnikov, B. N. Wan, M. Stamp, and JET EFDA Contributors, Nucl. Fusion **49**, 092002 (2009).
[45]D. A. D'Ippolito, J. R. Myra, and S. J. Zweben, Phys. Plasmas **18**, 060501 (2011).
[46]P. A. Robinson, Rev. Mod. Phys. **69**, 507 (1997).
[47]R. Rajaraman, *Solitons and Instantons: An Introduction to Solitons and Instantons in Quantum Field Theory* (Elsevier Science Publishers B.V., North-Holland, Amsterdam, 1989), pp. 105 and 112.
[48]Y. Z. Zhang and S. M. Mahajan, Phys. Fluids B **5**, 2000 (1993).
[49]P. W. Terry, Rev. Mod. Phys. **72**, 109 (2000).
[50]Y. Z. Zhang and S. M. Mahajan, Phys. Plasmas **24**, 054502 (2017).
[51]J. C. Hillesheim, E. Delabie, H. Meyer, C. F. Maggi, L. Meneses, E. Poli, and JET Contributors, Phys. Rev. Lett. **116**, 065002 (2016).
[52]V. N. Tsytovich, *An Introduction to the Theory of Plasma Turbulence* (Pergamon Press Ltd., 1972).
[53]P. W. Anderson, Phys. Rev. **109**, 1492 (1958).
[54]P. Sheng, *Introduction to Wave Scattering, Localization and Mesoscopic Phenomena*, 2nd ed. (Springer, Berlin, Heidelberg, New York, 2006).
[55]T. Xie, Y. Z. Zhang, S. M. Mahajan, S. L. Hu, H. He, and Z. Y. Liu, Phys. Plasmas **24**, 102506 (2017).
[56]Z. Qiu, L. Chen, and F. Zonca, Nucl. Fusion **54**, 033010 (2014).